

Submitted to *ApJ*

A comprehensive study of GRB 070125, a most energetic gamma ray burst

Poonam Chandra^{1,2}, S. Bradley Cenko³, Dale A. Frail⁴, Roger A. Chevalier², Jean-Pierre Macquart^{1,5}, Shri R. Kulkarni⁵, Douglas C.-J. Bock⁶, Frank Bertoldi⁷, Mansi Kasliwal⁵, Derek B. Fox⁸, Paul A. Price⁹, Edo Berger^{10,11}, Alicia M. Soderberg^{10,11,12}, Fiona A. Harrison³, Avishay Gal-Yam¹³, Eran O. Ofek⁵, Arne Rau⁵, Brian P. Schmidt¹⁴, P. Brian Cameron⁵, Lennox L. Cowie¹⁵, Antoinette Cowie¹⁵, Katherine C. Roth¹⁶, Michael Dopita¹⁷, Bruce Peterson¹⁷, Bryan E. Penprase¹⁸

pc8s@virginia.edu

¹Jansky Fellow, National Radio Astronomy Observatory

²Department of Astronomy, University of Virginia, P.O. Box 400325, Charlottesville, VA 22904

³Space Radiation Laboratory, MS 220-47, California Institute of Technology, Pasadena, CA 91125

⁴National Radio Astronomy Observatory, P.O. Box O, Socorro, NM 87801

⁵Division of Physics, Maths and Astronomy, California Institute of Technology, Pasadena, CA 91125

⁶Combined Array for Research in Millimeter-wave Astronomy, P.O. Box 968, Big Pine, CA 93513

⁷Argelander- Institut für Astronomie, Auf dem Hügel 71, D-53121 Bonn, Germany

⁸Department of Astronomy and Astrophysics, Pennsylvania State University, 525 Davey Laboratory, University Park, PA 16802

⁹Institute for Astronomy, University of Hawaii, 2680 Woodlawn Drive, Honolulu, HI 96822

¹⁰Princeton University Observatory, Peyton Hall, Ivy Lane, Princeton, NJ 08544

¹¹Observatories of the Carnegie Institute of Washington, 813 Santa Barbara Street, Pasadena, CA 91101

¹²Hubble Fellow

¹³Benoziyo Center for Astrophysics, The Weizmann Institute of Science, Rehovot 76100, Israel

¹⁴Research School of Astronomy and Astrophysics, Australian National University, Mt Stromlo Observatory, via Cotter Rd, Weston Creek, ACT 2611, Australia

¹⁵Institute of Astronomy, University of Hawaii, 2680 Woodlawn Drive, Honolulu, HI 96822-1897

¹⁶Gemini Observatory, 670 N. Aohoku Place, Hilo, HI 96720

¹⁷Institute of Advanced Studies, The Australian National University, ACT2611, Australia

¹⁸Department of Physics and Astronomy, Pomona College, 610 N. College Ave Claremont CA 91711

ABSTRACT

We present a comprehensive multiwavelength analysis of the bright, long duration gamma-ray burst GRB 070125, comprised of observations in γ -ray, X-ray, optical, millimeter and centimeter wavebands. Simultaneous fits to the optical and X-ray light curves favor a break on day 3.78, which we interpret as the jet break from a collimated outflow. Independent fits to optical and X-ray bands give similar results in the optical bands but shift the jet break to around day 10 in the X-ray light curve. We show that for the physical parameters derived for GRB 070125, inverse Compton scattering effects are important throughout the afterglow evolution. While inverse Compton scattering does not affect radio and optical bands, it may be a promising candidate to delay the jet break in the X-ray band. Radio light curves show rapid flux variations, which are interpreted as due to interstellar scintillation, and are used to derive an upper limit of 2.4×10^{17} cm on the radius of the fireball in the lateral expansion phase of the jet. Radio light curves and spectra suggest a high synchrotron self absorption frequency indicative of the afterglow shock wave moving in a dense medium. Our broadband modeling favors a constant density profile for the circumburst medium over a wind-like profile (R^{-2}). However, keeping in mind the uncertainty of the parameters, it is difficult to unambiguously distinguish between the two density profiles. Our broadband fits suggest that GRB 070125 is a burst with high radiative efficiency ($> 60\%$).

Subject headings: gamma rays: bursts, hydrodynamics, radiation mechanisms: non-thermal, circumburst matter

1. Introduction

To understand the inner workings of gamma-ray burst (GRB) central engines, it is necessary to constrain their true energy release. If a redshift is known, the isotropic energy release in gamma-rays, $E_{\text{iso},\gamma}$, is a readily measurable quantity. The “energy crisis” brought on by implied energy releases of $> 10^{54}$ erg (e.g., Kulkarni et al. 1999; Fruchter et al. 1999) was resolved when it was realized that GRB blast waves are collimated with opening angles θ_j of 2-30° (Rhoads 1999; Sari et al. 1999; Stanek et al. 1999; Harrison et al. 1999). Thus the beaming-corrected gamma-ray energy release, E_γ , is smaller than $E_{\text{iso},\gamma}$ by a factor $\sim \theta_j^2/2$.

Whatever energy is not released in the prompt emission powers a relativistic blast wave that plows into the circumburst medium (CBM). Measuring the kinetic energy of this outflow,

E_K , is challenging because only a fraction of this energy is radiated. Several methods have been used in this endeavor (see Berger et al. 2003b). The simplest method, using only the X-ray afterglow light curve, was suggested by Kumar (2000), Freedman & Waxman (2001), and Berger et al. (2003a). Provided that the X-rays are predominately synchrotron and the electrons radiate in the cooling regime, this method yields the energy per unit solid angle and the fraction of the shock energy carried by electrons ϵ_e . For those afterglows with high quality multiwavelength data sets, a fit of the data can be made using models that describe the dynamics of jet/circumburst interaction and that calculate the expected synchrotron and inverse Compton emission (e.g., Panaiteescu & Kumar 2001; Yost et al. 2003a). Finally, for bright, long-lived afterglows, E_K can be measured more robustly using the late-time radio light curve. Months or in some cases years after the burst, the blast wave becomes sub-relativistic (i.e. Sedov self-similar evolution) and the outflow is expected to be quasi-spherical (e.g., Frail et al. 2000; Berger et al. 2004; Frail et al. 2005).

Early studies, based on these methods, suggested that the energy release of long-duration GRBs lies within a narrow range with a mean of $\sim 10^{51}$ erg (e.g. Frail et al. 2001; Berger et al. 2003a). There are several problems with this simple picture, however, and the true situation is likely more complicated. For example, energy input into the blast wave now appears to extend beyond the prompt emission and into the afterglow phase. This could be due either to a long-lived central engine or slow-moving ejecta that take a long time to reach the shock front (Zhang et al. 2006).

The simple pictures of collimated explosions has been challenged by *Swift* detected GRBs. Kocevski & Butler (2007) give an excellent summary of the difficulties and their implications for collimation-corrected energy release E_γ . If (for whatever reason) the *Swift* sample of bursts has no jet breaks then we are faced with a growing number of GRBs that (by virtue of inferred isotropic energy release) are hyper-energetic i.e. well in excess of the canonical 10^{51} erg (e.g., Burrows & Racusin 2007b; Cenko et al. 2006b; Frail et al. 2006). If accepted, these events would provide stringent tests of existing progenitor models.

In this paper, we present multiwavelength observations of GRB 070125. Its bright afterglow has allowed us to follow the GRB until day 350 and obtain the most extensive radio data in the *Swift* era, coupled with well-sampled X-ray and optical light curves indicative of a jet break. Together with the well characterized prompt emission extending beyond 1 MeV (Bellm et al. 2007), GRB 070125 is truly a rare event.

In §2 we provide details of observations for GRB 070125. In §3 we describe our results, and find evidence for a jet break in the optical and X-ray data. The radio spectra show evidence for evolution from an optically thick to an optically thin phase, while the radio light curves show short timescale variability that we ascribe to scintillation. We carry out

a straightforward analytic modeling and derive some physical parameters of the shock and the circumburst medium. Finally, we carry out a detailed model fit of the entire broadband dataset and summarize our results in §4. We discuss the energetics, environment, relevance of reverse shock emission, efficiency of the GRB and the inverse Compton scattering effects for GRB 070125 in §5. The main conclusions are listed in §6.

2. Observations

In this section, we present multiwavelength observations of GRB 070125. We supplement our data set with the measurements reported in literature (mostly notices from the Gamma-ray Burst Circulars Network¹).

2.1. Gamma-Ray Observations

GRB 070125 was discovered by the Inter Planetary Network (IPN) of GRB detectors at 07:20:45 UT 25 January 2007 (Hurley et al. 2007). Mars Odyssey (HEND and GRS), Suzaku (WAM), INTEGRAL (SPI-ACS), RHESSI and Konus-Wind, all observed this intense, ~ 70 s long, event (Fig. 1). The burst was not in the field of view of *Swift*. Four minutes later the burst fell into the Burst Alert Telescope (BAT) field of view (Hurley et al. 2007). The *Swift* BAT position was consistent with the position of the GRB as triangulated by IPN. The small error circle from the BAT position enabled follow-up observations to identify the bright X-ray (§2.2) and optical (§2.3) afterglow.

Because of the high-energy (up to 1 MeV) coverage provided by RHESSI, Konus-Wind, and Suzaku, tight constraints can be made on the prompt emission spectrum of GRB 070125. In particular, the gamma-ray fluence was much more accurately measured than a typical *Swift* GRB (with coverage of only ~ 300 keV). A detailed analysis of the high-energy properties of GRB 070125 has been performed by Bellm et al. (2007), who found that the spectrum is well fit by a Band model (Band et al. 1993) with a peak energy $E_p = 430$ keV and the power-law photon indices (as defined in Band model) of -1.14 and -2.11 below and above the peak energy, respectively. The resulting fluence in the 20 keV – 10 MeV band was 1.7×10^{-4} erg cm $^{-2}$.

¹http://gcn.gsfc.nasa.gov/gcn3_archive.html

2.2. X-ray observations

The X-ray Telescope (XRT; Burrows et al. 2005a) on board *Swift* began observing the field of GRB 070125 46 ks after the burst trigger (Racusin & Vетere 2007). Due to the relatively low source flux, observations were conducted exclusively in Photon Counting (PC) mode, and so the effects of photon pile-up were negligible. During the first five orbits, the X-ray spectrum is well-fit by a power-law model with a photon index $\Gamma = 2.1 \pm 0.3$ ($N(\gamma) \propto \gamma^{-\Gamma} d\gamma$, where N is the photon flux density, Racusin & Vетere 2007). The inferred absorption is consistent with the Galactic absorption value of $N_{\mathrm{H}} \approx 8 \times 10^{20} \mathrm{cm}^{-2}$ (Racusin & Vетere 2007). The XRT continued to monitor the X-ray afterglow of GRB 070125 over the course of the next two weeks, until the source faded below the XRT sensitivity threshold.

Motivated by the enormous isotropic energy release of the prompt emission (§3.1) and the proposed lack of X-ray jet breaks observed in the *Swift* era (Burrows & Racusin 2007b), we obtained Director's Discretionary time on the *Chandra X-ray Observatory* to observe the X-ray afterglow of GRB 070125 at very late times. We obtained a 30 ks exposure using the Advanced CCD Imaging Spectrometer on board (Garmire et al. 2003) beginning at 21:28 UT 2007 March 5 (~ 40 d after the burst trigger). No source was detected at the position of the X-ray afterglow at this time. Formally, using a circular aperture with a one-arcsecond diameter, we detect 0.9 ± 5.0 photons in the energy range from 0.3 – 10 keV at the location of GRB 070125 (a $5 - \sigma$ upper limit).

The log of X-ray observations and the measured fluxes are summarized in Table 1. The *Swift* XRT light curve is obtained from the on-line repository² (Evans et al. 2007). We converted counts to flux using spectral parameters derived from the first five XRT orbits. We then converted the 0.3 – 10.0 keV flux to a flux density ($F_{\nu} \propto \nu^{-\beta}$, where $\beta = \Gamma - 1 = 1.1$) at $E = 1.486$ keV ($\nu_0 = 3.594 \times 10^{17}$ Hz). This value was so chosen that the flux was equally divided below and above this cutoff.

2.3. Optical observations

In response to the IPN-*Swift* localization, we began observing the field of GRB 070125 with the automated Palomar 60-inch telescope (P60; Cenko et al. 2006a) on the night of 2007 January 26. Inspection of the first images revealed a bright, stationary source at $\alpha = 07^{\mathrm{h}}51^{\mathrm{m}}17\overset{\mathrm{s}}{.}75$, $\delta = +31^{\circ}09'04\overset{\mathrm{s}}{.}2$ (J2000.0), not present in the Sloan Digital Sky Survey (SDSS) images of the field (Adelman-McCarthy et al. 2007). This position was promptly

²http://www.Swift.ac.uk/xrt_curves

reported as the afterglow of GRB 070125 (Cenko & Fox 2007), allowing several groups to obtain spectroscopy of the afterglow while still quite bright ($R \sim 18$ mag).

The optical afterglow of GRB 070125 was observed by a variety of facilities worldwide, as it turned out to be one of the brightest optical afterglows ever detected for a GRB (Updike *et al.*, in prep.) We continued to monitor the afterglow of GRB 070125 with the P60 in the Kron R and Sloan i' filters for the following four nights, until the afterglow faded below our sensitivity limit. All P60 data were reduced using our custom software pipeline (see Cenko *et al.* 2006a for details) using IRAF³ routines.

In addition to our P60 monitoring, we obtained three epochs of late-time optical photometry with the Gemini Multi-Object Spectrograph and Imager (GMOS; Hook *et al.* 2003) mounted on the 8-m Gemini North telescope. All three epochs consisted of either single r' or i' exposures obtained as acquisition images for spectroscopic observations. All GMOS images were reduced using the IRAF `gemini` package.

Finally, we obtained a single epoch of simultaneous g - and R -band imaging on the night of 2007 February 16 with the Low-Resolution Imaging Spectrometer (LRIS; Oke *et al.* 1995) mounted on the 10-m Keck Telescope. Individual images were bias-subtracted and flat-fielded using standard IRAF routines. Co-addition was performed using Swarp⁴. Photometric calibration for all of our optical imaging was performed relative to the SDSS, with empirical filter transformations from Jordi *et al.* (2006) applied where necessary. Typical RMS photometric uncertainties were ≈ 0.05 mag in all of our images.

Garnavich *et al.* (2007) imaged the position of the GRB 070125 afterglow with the LBC-blue CCD camera and 8.4-m SX mirror on the LBT on 2007 February 21.1 (UT) in r-band. A faint source is detected at the position of the afterglow with brightness $r=26.3 \pm 0.3$ mag. Since the source may be contaminated by the host galaxy, this observation represents an upper-limit on the magnitude of the afterglow 26.8 days after the GRB.

To convert magnitudes to flux densities, we used zeropoint measurements from Fukugita *et al.* (1995). We have incorporated a modest amount of Galactic extinction ($E(B-V) = 0.052$; Dickey & Lockman 1990; Schlegel *et al.* 1998) into these results. The results of our optical monitoring of GRB 070125, together with measurements reported by other observatories via the GCN, are shown in Table 2.

³IRAF is distributed by the National Optical Astronomy Observatory, which is operated by the Association for Research in Astronomy, Inc., under cooperative agreement with the National Science Foundation.

⁴<http://terapix.iap.fr>

2.4. Millimeter & Sub-Millimeter observations

We obtained director's discretionary time for observations in the 1.2-mm band (250 GHz) at the Max-Planck Millimeter Bolometer Array (MAMBO), installed at the IRAM 30 m telescope on Pico Veleta, Spain. We used the MAMBO-2 version with 117 channels. The bandwidth used was 210 – 290 GHz half power. Our first observations took place on 2007 January 30 and we detected the afterglow of GRB 070125 at a flux density of 3.14 ± 0.59 mJy. We monitored the afterglow regularly until it had dropped below the instrumental sensitivity.

Observations were also obtained at 95 GHz using the Combined Array for Research in Millimeter-wave Astronomy (CARMA)⁵, in good weather on 2007 February 5, 9, 12, and 18. Individual observations were between 6.7 – 8 hours in length. System temperatures ranged from 200 to 400 K, scaled to outside the atmosphere. A single linear polarization was received in a bandwidth of 1.2 – 1.5 GHz per sideband, depending on the antenna. CARMA was in the C configuration, with baselines 26 – 370 m.

The bright quasar 0748+240 was observed as a phase calibrator at 20-minute intervals. A fainter source nearer GRB 070125, 0741+312 (2° distant), was observed for 30 seconds after each observation of the GRB. The flux density of this source when self-calibrated was compared to the flux density when calibrated with 0748+240. The ratio of these measurements provides an estimate of the atmospheric decorrelation affecting the observations. The measured flux densities of GRB 070125 were corrected by this factor, which ranged from 9 to 14%. The absolute flux density scale was derived from observations of Uranus on February 2 and 19, and transferred by reference to the quasar 3C84, which was observed on those dates and near the beginning of each observation of GRB 070125.

Images were made for each observation using the MIRIAD software package (Sault, Teuben, & Wright 1995). The quoted uncertainty in the measurement is dominated by the sensitivity of the map, but also includes an estimate for the flux density scale uncertainty of 15%. We detected the afterglow in the first three observations. The flux density of the mean observation time 2007 February 5, 0700 UT was 2.3 mJy. The log and flux densities of the MAMBO and CARMA observations can be found in Table 3.

⁵Support for CARMA construction was derived from the Gordon and Betty Moore Foundation, the Kenneth T. and Eileen L. Norris Foundation, the Associates of the California Institute of Technology, the states of California, Illinois, and Maryland, and the National Science Foundation. Ongoing CARMA development and operations are supported by the National Science Foundation under a cooperative agreement, and by the CARMA partner universities.

2.5. Centimeter band observations

The earliest measurement of the radio flux density was taken from the Westerbork Synthesis Radio Telescope (WSRT) in 5 GHz band by van der Horst (2007)), just 1.5 days after the burst. A $2-\sigma$ upper limit on the 5 GHz flux density of $F_\nu < 174 \mu\text{Jy}$ was obtained. Shortly thereafter, we triggered Very Large Array (VLA) observations of the field. Our first measurement at 8.46 GHz, four days after the explosion, resulted in a strong detection ($F_\nu = 360 \pm 42 \mu\text{Jy}$; Chandra & Frail 2007). Encouraged by this detection, we triggered observations with the Giant Meterwave Radio Telescope (GMRT) in the 610 MHz band on 2007 January 31. However, we did not detect the afterglow with the GMRT to a $2-\sigma$ limiting flux density of $F_\nu < 300 \mu\text{Jy}$ (Chandra et al. 2007).

We continued the followup observations of GRB 070125 with the VLA from 2007 January 29th until 2007 February 2nd at 8.46 GHz and 4.86 GHz. After 2007 February 5, we undertook observations in the 1.46, 4.86, 8.46, 14.94 and 22.5 GHz bands. We followed the GRB until day 342 since explosion.

Each observation at a single frequency was from 30 minutes to one hour duration. The bright radio quasar 3C48 (0137+331) was used as a flux calibrator. We used phase calibrators 0745+317 and 0741+312 to track the instrumental and/or atmospheric gain and phase variations, as well as to monitor the quality and the sensitivity of the data. A bandwidth of 2×50 MHz was used for all the observations. The data were analyzed using standard data reduction procedures within the Astronomical Image Processing System (AIPS). During initial observations, the VLA was in “C→D” and “D” array configuration for early observations; because of the short baselines, there were many sources in the field of view at lower frequencies. For such cases at 4.86 and 1.43 GHz, we did 3-D cleaning with several rounds of self-calibration inside AIPS.

On 2007 February 7, 8 and 14, we made longer observations for durations of ~ 5.5 , ~ 4 , and ~ 8 hours, respectively, in order to search for variability due to Interstellar Scintillation (ISS) (see §3.2). We combined every 20 minutes of the data and imaged the afterglow field of view to measure short timescale scintillations. The results of our radio monitoring of the afterglow of GRB 070125 can be found in Table 3.

3. Results

In this section, we carry out a simple analysis with minimum model assumptions to derive robust conclusions. We find strong evidence for a jet break in the combined fitting of the X-ray and the optical light curves (§3.1). In §3.2 we use the radio scintillation data to

constrain the size of the emitting region. Together, the jet break time and the inferred radius allow us to constrain the prompt energy release (§3.3) and the density of the circumburst medium (§3.4). In the next section (§4), we undertake a detailed analysis utilizing the full machinery of afterglow models.

3.1. Break in the Light Curve

We performed a joint fit on the R , i' , and X-ray light curves of GRB 070125 using both a single power-law (spl) and a broken power-law (bpl) model. The results of these two fits are shown in Figure 2 and Table 4. We also perform the spl and the bpl fits letting the X-ray and optical pre-break indices vary independently. The results are consistent with the previous fits in which we constrained both the indices to be the same. Altogether, the broken power-law model, indicating a jet break at $t_j = 3.8$ d, is strongly favored ($\chi^2_{\text{r}}(\text{bpl}) = 1.30$ for 97 d.o.f. vs. $\chi^2_{\text{r}}(\text{spl}) = 2.23$ for 99 d.o.f.).

We note, however, that the distinction between the two models is significantly more pronounced in the optical ($\chi^2_{\text{r}}(R\text{-band, bpl}) = 1.54$ for 52 d.o.f. vs. $\chi^2_{\text{r}}(R\text{-band, spl}) = 2.22$ for 52 d.o.f.; and $\chi^2_{\text{r}}(i'\text{-band, bpl}) = 0.77$ for 25 d.o.f. vs. $\chi^2_{\text{r}}(i'\text{-band, spl}) = 3.43$ for 52 d.o.f.) than the X-rays. As first noted by Burrows & Racusin (2007a), without the late-time *Chandra* data, the X-ray light curve cannot distinguish between the spl and bpl models. Formally, we find the single power-law model is actually favored in the X-rays ($\chi^2_{\text{r}}(\text{X-ray, spl}) = 0.88$ for 22 d.o.f. vs. $\chi^2_{\text{r}}(\text{X-ray, bpl}) = 1.32$ for 20 d.o.f.). This could perhaps be due to the denser sampling at early times.

We also perform independent optical and X-ray fitting. The optical fits are consistent with our joint fits. However, when we fit the X-ray light curve independently of the optical, the jet break appears much later, $t_j \approx 9$ d (Fig. 2). While not formally required by our simple analysis, we consider the possibility that this break may in fact be *chromatic*. We discuss this further in §5.

3.2. Scintillation and fireball size

As can be seen in Fig. 3 and Table 3, there are significant day-to-day deviations in the low frequency radio light curves. These modulations are likely due to scintillation caused by interstellar propagation effects.

We obtained long-duration observations of the afterglow of GRB 070125 at 8.5 GHz on three separate occasions: February 7 (5.5 hour duration), February 8 (4 hour duration),

and February 14 (8 hour duration). The data were split into 20 minute blocks and imaged in order to extract information on the fast variability of the source. GRB 070125 exhibits flux density variations with a significance exceeding 99.8% on each of the three epochs (see Fig. 4). The reduced χ^2 values for the hypothesis of no variability are 2.31 (with 17 degrees of freedom), 4.42 (10 d.o.f.) and 2.84 (23 d.o.f.) for the three dates, respectively.

We used intensity structure functions to determine the variability timescale on each date. While the short baseline hindered a definitive determination, we tentatively identify breaks at $\Delta T \approx 6 \times 10^3, 7 \times 10^3$ and 9×10^3 s, in the three structure functions. The breaks are marginally significant in the data from 7 February and 8 February, but not so prominent in the 14 February images. This can be explained by quenching of the scintillation as the source expands at late times. These measurements are congruent with the timescales of the peaks and troughs apparent in the corresponding centimeter-wavelength lightcurves (Fig. 3).

The interpretation of the variability depends on whether the scintillation occurs in the weak or strong regime. Strong scintillations require that the so-called Fried parameter (coherence length scale, s_d) be smaller than the Fresnel size (r_F). Strong chromatic scintillations is possible only for sources smaller than λ/s_d . These lead to the following two conditions (Goodman 1997):

$$\nu < 13.4 \left(\frac{\text{SM}}{10^{-3.19} \text{m}^{-20/3} \text{kpc}} \right)^{6/17} \left(\frac{D_{\text{scr}}}{\text{kpc}} \right)^{5/17} \text{GHz} \equiv \nu_{\text{ss}} \quad (1)$$

$$\theta_d = 6.5 \left(\frac{\nu}{8.46 \text{ GHz}} \right)^{-11/5} \left(\frac{\text{SM}}{10^{-3.19} \text{m}^{-20/3} \text{kpc}} \right)^{3/5} \mu\text{as} \ll \sqrt{\frac{c}{2\pi\nu D_{\text{scr}}}}, \quad (2)$$

where SM is the scattering measure and D_{scr} is the effective distance to the scattering material. To determine this, we first estimate the scattering distance and the scattering measure using the formulation of Cordes & Lazio (2002). Given the Galactic coordinates of GRB 070125, $(l, b) = (189.4, 25.6)$, the expected SM is $10^{-3.19} \text{m}^{-20/3} \text{kpc}$ and the effective distance to the scattering material is $D_{\text{scr}} = 0.84 \text{kpc}$. For these parameters, the critical frequency obtained from Eq. 1 is 12.7 GHz. These parameters also satisfy the condition of Eq. 2. Hence, the GRB is likely to be in the strong scintillation regime. However, given the paucity of our knowledge of the distribution of scattering material off the Galactic plane, these estimates should be taken with caution.

Strong scintillation can be diffractive as well refractive in nature. Diffractive scintillation of a point-like source is characterized by variations with a modulation index (m_p) close to unity, where the modulation index is a measure of how much the modulated flux varies around its intrinsic flux density level. The size limit for a source to exhibit diffractive scintillation

(θ_1) is (Goodman 1997):

$$\theta_1 = 1.2 \left(\frac{\nu}{8.46 \text{ GHz}} \right)^{6/5} \left(\frac{D_{\text{scr}}}{\text{kpc}} \right)^{-1} \left(\frac{\text{SM}}{10^{-3.19} \text{ m}^{-20/3} \text{ kpc}} \right)^{-3/5} \mu\text{as}. \quad (3)$$

For actual size of the source, $\theta_s, \theta_s \leq \theta_1$. Diffractive scintillation occurs when $\theta_d > \theta_1$, which is indeed the case for GRB 070125 using the parameters discussed above.

We now attempt to limit the size of the emitting region using the formulation of diffractive scintillation (Walker 1998, 2001; Cordes & Lazio 2002), but with more robust estimates of D_{scr} and SM. The timescale of diffractive scintillation can be expressed as:

$$t_{\text{diff}} = 5950 \left(\frac{\nu}{8.46 \text{ GHz}} \right)^{6/5} \left(\frac{\text{SM}}{10^{-3.19} \text{ m}^{-20/3} \text{ kpc}} \right)^{-3/5} \left(\frac{v_{\text{ISS}}}{30 \text{ km s}^{-1}} \right)^{-1} \text{ s}, \quad (4)$$

where v_{ISS} is the speed of the scattering material transverse to the line of sight. The decorrelation bandwidth ($\Delta\nu_{\text{dc}}$) for diffractive scintillation is then (Goodman 1997):

$$\Delta\nu_{\text{dc}} = 1.55 \left(\frac{\nu}{8.46 \text{ GHz}} \right)^{22/5} \left(\frac{D_{\text{scr}}}{\text{kpc}} \right)^{-1} \left(\frac{\text{SM}}{10^{-3.19} \text{ m}^{-20/3} \text{ kpc}} \right)^{-6/5} \text{ GHz}. \quad (5)$$

Using the variability timescale of $\Delta T \sim 7 \times 10^3 \text{ s}$ measured on 8 February, along with $v_{\text{ISS}} = 30 \text{ km s}^{-1}$, we infer a scattering measure of $SM = 0.76 \times 10^{-3.19} \text{ m}^{-20/3} \text{ kpc}$. In Eq. 5 we take the decorrelation bandwidth to be roughly half of the frequency of observation, i.e. $\Delta\nu_{\text{dc}} \approx (1/2) \times \nu$, because at the boundary of strong and weak scintillation $\Delta\nu_{\text{dc}} \approx \nu$ (Goodman 1997). This yields a distance to the scattering screen of $D_{\text{scr}} = 0.51 \text{ kpc}$.

Knowing these two parameters, we can put an upper limit on the angular size of the emitting region of $\theta_{\text{src}} = 2.8 \mu\text{as}$. At $z = 1.547$ (Cenko et al. 2007), this translates⁶ to a linear size of $4.7 \times 10^{17} \text{ cm}$ or a radius of $2.4 \times 10^{17} \text{ cm}$. We caution that the foregoing estimates are rough both because the timescale ΔT is poorly determined and the lightcurves are poorly sampled.

Variability due to refractive scintillation is expected at late stages, even after the source has expanded sufficiently. Refractive scintillations are expected to be broadband in nature and start dominating once diffractive scintillations are quenched. The source exhibited refractive scintillation during the two months subsequent to 2007 February 8, as can be seen from the first 70 days of the 8.46 GHz data plotted in Figure 3.

⁶All the calculations were done with $H_0 = 71$, $\Omega_m = 0.27$ and $\Omega_{\text{vac}} = 0.73$.

In a standard GRB afterglow model, the jet starts to spread sideways after the jet break (Piran 1999, 2005a; Meszaros 2006). During this stage, the fireball size remain constant. Once the jet has become spherical, it reaches the non-relativistic regime. In this regime, the equations of motion follow self-similar Sedov-Taylor solutions. Thus, this estimate represents the size of the fireball in the post jet break regime until the expansion becomes sub-relativistic, which occurs between days 30 and 50.

3.3. Energetics

The isotropic gamma ray energy of a GRB can be written as:

$$E_{\gamma, \text{iso}} = 3 \times 10^{51} \text{ erg} \left(\frac{2}{1+z} \right) \left(\frac{d_L}{7.12 \text{ Gpc}} \right)^2 \left(\frac{f_\gamma}{10^{-6}} \right),$$

where d_L is the luminosity distance of the GRB and f_γ is total fluence. The fluence in the 20 keV – 10 MeV energy range is $1.74 \times 10^{-4} \text{ erg cm}^{-2}$ (Golenetskii et al. 2007; Bellm et al. 2007), yielding $E_{\gamma, \text{iso}} = 1.06 \times 10^{54} \text{ erg}$. This is one of the largest isotropic energy releases (top 1%) ever reported for a GRB (Amati 2006).

To determine the true prompt energy release, this isotropic value needs to be corrected for collimation. The combined fit to the optical and X-ray data gave a jet break at $t_j \approx 3.78$ day (§3.1). The collimation correction depends on the density profile of the circumburst medium. We derive corrections for a uniform density (ISM; $n = \text{constant}$) medium and a wind-like (wind; $n = Ar^{-2}$; $A = 3 \times 10^{35} A_\star \text{ cm}^{-1}$) medium (Wu et al. 2005, and references therein). The collimation angle for a radiative afterglow can be written as (Sari et al. 1998; Frail et al. 2001; Li & Chevalier 2003):

$$\theta_j(\text{ISM}) = 0.20 \left(\frac{t_j}{1 \text{ day}} \right)^{3/7} \left(\frac{2}{1+z} \right)^{3/7} \left(\frac{\Gamma_0}{200} \right)^{1/7} \left(\frac{E_{52}}{n} \right)^{-1/7} \quad (6)$$

$$\theta_j(\text{Wind}) = 0.50 \left(\frac{t_j}{1 \text{ day}} \right)^{1/3} \left(\frac{2}{1+z} \right)^{1/3} \left(\frac{\Gamma_0}{200} \right)^{1/3} \left(\frac{E_{52}}{A_\star} \right)^{-1/3}. \quad (7)$$

where t_j is the break in the optical light curve in days, and E_{52} is the isotropic kinetic energy of the fireball in units of 10^{52} erg . The term Γ_0 is the initial Lorentz factor of the fireball.

Similarly, the size of the spherical fireball can be expressed in the ISM and wind media as (Sari et al. 1998; Li & Chevalier 2003):

$$R(\text{ISM}) = 1.3 \times 10^{17} \left(\frac{E_{52}}{n} \right)^{2/7} \left(\frac{\Gamma_0}{200} \right)^{-2/7} \left(\frac{1+z}{2} \right)^{-1/7} t_{\text{days}}^{1/7} \text{ cm} \quad (8)$$

$$R(\text{Wind}) = 0.17 \times 10^{17} \left(\frac{E_{52}}{A_*} \right)^{2/3} \left(\frac{\Gamma_0}{200} \right)^{-2/3} \left(\frac{1+z}{2} \right)^{-1/3} t_{\text{days}}^{1/3} \text{ cm}, \quad (9)$$

which after jet break in GRB 070125 translates to:

$$R(\text{ISM}) = 1.3 \times 10^{17} \left(\frac{E_{52}}{n} \right)^{1/3} \left(\frac{\Gamma_0}{200} \right)^{-1/3} \left(\frac{\theta_j}{0.2} \right)^{1/3} \text{ cm} \quad (10)$$

$$R(\text{Wind}) = 0.17 \times 10^{17} \left(\frac{E_{52}}{A_*} \right) \left(\frac{\Gamma_0}{200} \right)^{-1} \left(\frac{\theta_j}{0.5} \right) \text{ cm}. \quad (11)$$

Using the emission radius derived from scintillation studies ($R \leq 2.4 \times 10^{17} \text{ cm}$), we find an opening angle of $\theta \leq 0.25 \text{ rad}$ (14°) for the ISM model and $\theta \leq 0.23 \text{ rad}$ (13°) for the wind model. The Lorentz factor of the shocked ejecta at the time of jet break is $\gamma(t_{\text{jet}}) \cong 1/\theta = 4$ in the ISM model and 5 in the wind model.

3.4. Circumburst density

From Eq. (10) and (11), the circumstellar density can be written in terms of the kinetic energy of the afterglow as $n \geq E_{52}/0.11 \text{ cm}^{-3}$ and $A_* \geq E_{52}/1.54$ for the ISM and the wind models, respectively. Let η_γ be the efficiency factor for converting the fireball energy into the radiation energy, i.e. $\eta_\gamma = E_\gamma/(E_\gamma + E_K)$. For an empirical value of $\eta_\gamma = 0.35$ (Frail et al. 2003), the number density of GRB 070125 is $n \approx 50 \text{ cm}^{-3}$ in the ISM model and $A_* \approx 2.5$ in the wind model. This value is quite high, even for GRBs, and indicates that the afterglow of GRB 070125 is expanding into a dense medium.

A natural consequence of a high circumburst density is a high synchrotron self-absorption frequency. To this end, we plot broadband radio spectra (Figure 5). To improve the signal-to-noise ratio, we binned the spectra into 4 groups ($t = 6 - 17 \text{ d}$, $18 - 35 \text{ d}$, $56 - 86 \text{ d}$, and $160 - 200 \text{ d}$). The division was initially done on the basis of similarly-looking spectra, but later in this section we justify it by demonstrating that the spectral evolution has a weak time dependence. As can be seen, there is a clear turnover in the spectra in the first three epochs. Moreover, there is some indication that the turnover frequency evolves to lower frequencies with time. At the last epoch, no turnover frequency is discernible and the spectrum is inverted.

This spectral behavior has been seen in many previously well-studied GRB afterglows. We interpret this behavior in terms of the evolution of the afterglow from an optically thick to optically thin phase, parametrized by a single unknown, the synchrotron self-absorption frequency ν_a . We can measure the value of ν_a from the radio spectra using a very simple

formulation given below:

$$F_\nu = \begin{cases} F_{\max} \left(\frac{\nu}{\nu_a} \right)^2, & \nu < \nu_a, \\ F_{\max} \left(\frac{\nu}{\nu_a} \right)^{\frac{1}{3}}, & \nu > \nu_a. \end{cases} \quad (12)$$

The above relation is a broken power-law with a break at ν_a . We used the following smooth approximation of eq. (12):

$$F_\nu = F_{\max} \left(\frac{\nu}{\nu_a} \right)^2 \left[1 + \left(\frac{\nu}{\nu_a} \right)^{2-\frac{1}{3}} \right]^{-1} \quad (13)$$

We fit this function to the first three radio spectra and obtain the following values of synchrotron self-absorption frequency:

$$\begin{aligned} \nu_a &= 12.25^{+1.70}_{-0.92} \text{ GHz in the range } 6 - 17 \text{ days,} \\ \nu_a &= 11.22^{+1.00}_{-0.61} \text{ GHz in the range } 18 - 35 \text{ days,} \\ \nu_a &= 7.49^{+0.36}_{-0.28} \text{ GHz in the range } 56 - 86 \text{ days.} \end{aligned}$$

Our approximation of a constant ν_a within each epoch is justified because of the slow evolution of ν_a . The best fit time dependence to the values given above is $\nu_a \propto t^{-0.24 \pm 0.05}$. The spectrum in the final epoch was well into the optically thin phase so we could not determine ν_a at this epoch.

We also plot the multiwaveband spectra on day 10.7 and day 23.4 (Fig. 6), the two epochs at which we had observations in all the bands simultaneously. This shows radio data points to be on the optically thick part of the spectra. The afterglow peaks at 3-mm band and the optical and X-ray data fall in the optically thin regime. This gives a rough estimate of the break frequencies, ν_m , corresponding to the minimum electron Lorentz factor, and ν_c , the cooling frequency. We also plot νF_ν , a measure of energy, against ν . The curve peaks at the cooling frequency ν_c (Fig. 6).

4. Broadband Modeling

In the previous section, we used simple analytical techniques to estimate four fundamental physical properties of the explosion: the opening angle ($\theta \approx 0.23 - 0.25$ radian), the size of the emitting region ($R \approx 2.4 \times 10^{17}$ cm), the collimation-corrected prompt energy release ($E_\gamma \approx 3 \times 10^{52}$ erg), and the circumburst density ($n \approx 50 \text{ cm}^{-3}$; $A_* \approx 2.5$). Here we combine *all* our observations of the GRB 070125 afterglow in an attempt to derive a

comprehensive model of the entire afterglow evolution. Our modeling software assumes a standard synchrotron forward shock formulation, with possible contributions from inverse Compton (IC) emission and radiative losses also included. Full details can be found in Yost (2004) and Yost et al. (2003a).

As in §3.1, we ignore all data before $t = 1$ d due to the possibility of late-time energy injection. Based on our results in §3.2, we have incorporated scintillation effects into the radio regime. We used an LMC-like extinction model for the optical data (Pei 1992); however, the extremely small host contribution to the extinction makes the effects of differing extinction laws negligible.

4.1. Wind Model

Results of the best fit wind model parameters are tabulated in Table 5. In terms of χ^2 and the model-fit statistic⁷, the wind model does a slightly better job than the ISM model. However, the resulting best-fit parameters for the wind model are either unphysical (i.e. ϵ_e , the fractional energy imparted to electrons in the shock, approaching unity) or quite different from the values we derived in §3. The extremely small isotropic afterglow kinetic energy ($E_{52} \approx 0.3$) compared to the γ -ray isotropic energy is also troubling (the same is true in the ISM case, but to a lesser extent). We also notice that the wind model is less stable to small changes in the parameter space.

We fit the wind model with and without the inverse Compton effects. The model without inverse Compton effect gives even more unphysical values with many of the parameters asymptotically reaching very high values. The magnetic field fraction required reaches 100% in this model.

Apparently allowing ϵ_e be a free parameter is problematic. We fixed ϵ_e to be 0.4 and obtained a good fit (see Table 5). This exercise demonstrates that microphysical parameters are not constrained by our observations, at least for wind model.

4.2. ISM Model

The best-fit results for the ISM model are also provided in Table 5. The ISM model gives values of various parameters closer to the ones obtained from our simple analytical

⁷ $-\ln(P) = 0.5 \times (\chi^2 + 2\sum \ln(\sigma_i)) + \text{constant}$, here P is the probability function and σ_i is standard deviation

models. The jet break time, density scale, and collimation angle are in good agreement with our previous results.

The energy quoted in Table 5 is the isotropic blastwave energy at the time when $\nu_c = \nu_m$, i.e. at the time of the transition from fast cooling to slow cooling ($t \sim 8$ d in our model). This isotropic kinetic energy is much smaller than the isotropic gamma-ray energy obtained from the Konus-Wind/RHESSI fluence (§3.3). This may indicate that either there are high radiative losses at early times or the prompt emission is rather efficient with an extremely high value of η_γ .

4.3. Broadband Model Results and Interpretation

We plot the results of our broadband modeling in Figures 7, 8, and 9. It is difficult to differentiate between the wind and the ISM models purely on the basis of these plots. Both models represent the optical data fairly well at early times (Fig. 7). At late times ($t > 4$ d), both models over-predict the *R*-band flux, though with significantly less discrepancy in the constant density medium. IC effects are negligible in optical bands.

In the radio bands, none of the models fit particularly well, especially at early times (< 15 days). This is likely caused partly by the diffractive scintillation (§3.2). IC scattering has no influence in this band. The most puzzling behavior is revealed in the 4.8 GHz band. An early detection at $t \approx 4$ d, both in our data and the WSRT van der Horst (2007), is followed by almost two weeks of non-detections. Summing all these non-detections, we can put very strict limits on the 4.8 GHz flux at this time: $f_\nu < 71 \mu\text{Jy}$. The reason for this drop in flux is unclear, for it cannot be due to scintillation. We consider the possibility that the early detection is due to the reverse shock emission, in §5.

In Figure 8, we plot the broadband spectra from radio to X-ray at various times of the afterglow evolution. They are represented well with our models. Both the wind and ISM environments seem to do an equally good job.

We plot the X-ray light curve of GRB 070125 in Figure 9. This is the only band affected by IC emission. In the upper panel of Figure 9, we plot the model assuming only synchrotron radiation, while the lower panel incorporates IC scattering as well. The wind model in a pure synchrotron fit has very unphysical parameters (Table 5); hence we do not consider it further. In the ISM model, the observations at $4 \lesssim t \lesssim 10$ d do not fit the data very well without any IC emission. The fit improves significantly for both environments when we incorporate IC effects. The IC component seems to raise the X-ray flux roughly almost the same time the jet break becomes visible in the optical bands. This could well explain the

jet break at a later stage in the X-rays. We will discuss this further in §5.

5. Discussion

With our comprehensive broadband models in hand, we now turn to some of the questions raised in the previous sections.

5.1. Is Inverse Compton scattering delaying the jet-break?

Here we examine the IC scattering effect on the GRB afterglow lightcurve in the X-ray band. We adapt an approach in which we use only the synchrotron model for the GRB afterglow and derive various parameters such as E , p , ϵ_e , ϵ_B , density etc from the broadband data fitting. In this approach, we force the broadband jet break to be fixed on the day of the optical jet break from our analytical fits i.e. on day 3.7. We then use these parameters to derive the light curve purely due to IC effect. For reasons noted earlier we confine our discussion to the ISM model. Here, we assume that the spectrum due to IC scattering has the same shape as that of the synchrotron model. Hence, IC spectrum in the X-ray band is

$$F_\nu^{\text{IC}} = \begin{cases} F_{\text{max}}^{\text{IC}} \left(\frac{\nu}{\nu_c^{\text{IC}}} \right)^{-1/2}, & \nu_c^{\text{IC}} < \nu < \nu_m^{\text{IC}}, \\ F_{\text{max}}^{\text{IC}} \left(\frac{\nu}{\nu_m^{\text{IC}}} \right)^{-p/2} \left(\frac{\nu_m^{\text{IC}}}{\nu_c^{\text{IC}}} \right)^{-1/2}, & \nu > \nu_m^{\text{IC}}, \end{cases} \quad (14)$$

Here $F_{\text{max}}^{\text{IC}}$ is IC peak flux, ν_c^{IC} is IC cooling frequency and $\nu > \nu_m^{\text{IC}}$ is IC peak frequency.

The best fit parameters from the synchrotron broadband model fit are: $E_{52} = 2.98$, $\theta_j = 0.23$ rad, $p = 2.27$, $n = 15.7 \text{ cm}^{-3}$, $\epsilon_e = 0.275$, $\epsilon_B = 0.274$, $t_c = 7.8 \text{ d}$ and $t_j = 3.7 \text{ d}$. Here t_c is the transition time from the fast cooling to the slow cooling state. E_{52} is the isotropic-equivalent kinetic energy at $t = t_c$. IC scattering delays the cooling time by a fraction $(1 + \epsilon_e/\epsilon_B)^2$ (Sari & Esin 2001), i.e. the cooling time in presence of the IC effect is $t_c^{\text{IC}} = 31 \text{ d}$. Thus, for the time span of our observations, the afterglow remains in the fast cooling state and we will use formulation in this regime.

Using the formulation described in Sari & Esin (2001) and Wei & Lu (1998), we estimate the time (t_{IC}) when IC scattering starts becoming important at 1.486 keV (the X-ray light curve frequency). Using above best fit parameter values, we obtain $t_{\text{IC}} = 2.8 \text{ day}$. The IC light curve will satisfy the pre-jet break condition in the timerange of $t_{\text{IC}} \leq t \leq t_{\text{jet}}$, i.e.

between day $2.8 - 3.7$. The light curve will follow post-jet break formulation from day 3.7 onwards.

The flux density, size, Lorentz factor and cooling frequencies derived on day 2.8 are: $R = 2.86 \times 10^{17}$ cm, $F_{\max} = 24.2$ mJy, $\nu_m = 4.09 \times 10^{12}$ Hz and $\nu_c = 5.17 \times 10^{11}$ Hz. Hence, the derived IC parameters on day 2.8 are: $F_{\max}^{\text{IC}} = 0.024$ μ Jy, $\nu_m^{\text{IC}} = 2\gamma_m^2 \nu_m = 2.42 \times 10^{18}$ Hz, and $\nu_c^{\text{IC}} = 2\gamma_c^2 \nu_c = 23.9 \times 10^{16}$ Hz. Here γ_m and γ_c parameters are defined in Sari & Esin (2001). The time dependences of various parameters in the pre-jet break epoch are: $R \propto t^{1/4}$, $\Gamma \propto t^{-3/8}$, $F_{\max} \propto t^0$, $\nu_m \propto t^{-3/2}$, $\nu_c \propto t^{-1/2}$, $F_{\max}^{\text{IC}} \propto t^{1/4}$, $\nu_m^{\text{IC}} \propto t^{-9/4}$, and $\nu_c^{\text{IC}} \propto t^{-1/4}$. Our frequency of observation ($\nu = 3.59 \times 10^{17}$ Hz) satisfies $\nu_c^{\text{IC}} < \nu < \nu_m^{\text{IC}}$ condition at $t = 2.8$ d. Therefore, using Eq. 14, the 1.5 keV light curve for IC scattering between day $2.8 - 3.7$ becomes

$$F_{\nu}^{\text{IC}}(t) = 0.0079 \left(\frac{t}{2.8\text{d}} \right)^{1/8} \mu\text{Jy}. \quad (15)$$

From day 3.7 onwards, we use the post-jet break formulation and derive the IC light curve. The time dependences of various parameters in the post-jet break regime are: $R \propto t^0$, $\Gamma \propto t^{-1/2}$, $F_{\max} \propto t^{-1}$, $\nu_m \propto t^{-2}$, $\nu_c \propto t^0$, $F_{\max}^{\text{IC}} \propto t^{-1}$, $\nu_m^{\text{IC}} \propto t^{-3}$, and $\nu_c^{\text{IC}} \propto t^1$. On the jet break day, we find $\nu_m^{\text{IC}} = 1.29 \times 10^{18}$ Hz and $\nu_c^{\text{IC}} = 3.6 \times 10^{16}$ Hz, which still satisfies $\nu_c^{\text{IC}} < \nu < \nu_m^{\text{IC}}$ condition. Therefore, we derive the light curve from day 3.7 onwards using Eq. 14 as

$$F_{\nu}^{\text{IC}}(t) = 0.0082 \left(\frac{t}{3.7\text{d}} \right)^{-1/2} \mu\text{Jy}. \quad (16)$$

The IC frequency ν_m^{IC} reaches the X-ray observation frequency of $\nu = 3.594 \times 10^{17}$ Hz on day 5.7 . Hence, the above light curve is valid until day 5.7 .

After day 5.7 , the IC flux density in the $\nu > \nu_m^{\text{IC}}$ regime (Eq. 14), which gives the light curve in this regime as follows:

$$F_{\nu}^{\text{IC}}(t) = 0.0066 \left(\frac{t}{5.7\text{d}} \right)^{-2.4} \mu\text{Jy}. \quad (17)$$

Combining Eqs. (15), (16) and (17), we plot the total IC light curve in Fig. 10. The figure clearly shows that IC scattering flattens the light curve and delays the jet break to later time. What happens after day $9 - 10$ is unknown due to the lack of X-ray detection of the afterglow.

While we have strong evidence that IC effects delay the X-ray jet break in GRB 070125, we would like to know if this effect could be seen in other GRBs as well. In the pre-*Swift* era,

the X-ray data were not sufficiently well sampled to search for jet breaks, and so collimation corrections were almost exclusively calculated in the optical bands. In the *Swift* era, with a plethora of well-sampled XRT light curves, we may be missing the jet break due to IC effects in many GRBs. The radio afterglow is not useful in determining the jet break, since GRBs most likely scintillate in radio bands at such early times. This makes the optical the unique bandpass in which the real jet break can be determined unambiguously.

The inverse Compton effect is most prominent in a dense medium. Our radio observations have already shown that GRB 070125 resides in a very dense medium. It has been shown by Wei & Lu (2000) that IC is important in relativistic ejecta and even in non-relativistic ejecta in high density. Harrison et al. (2001) found good evidence for IC production of X-rays in GRB 000926 and derived a high circumburst density, 30 cm^{-3} , comparable to the density we find for GRB 070125. Corsi & Piro (2006) have shown that the late time flattening in the X-ray light curve of XRF 050406 can be explained as an effect of IC scattering. For inverse Compton scattering to play an important role, the electron energy density fraction (ϵ_e) must be larger than the magnetic energy density fraction (ϵ_B).

Recently, Panaiteescu (2007) has discussed chromatic breaks occurring due to scattering of the forward-shock synchrotron emission by a relativistic outflow located behind the leading blast-wave. This model may have X-ray jet breaks showing up at later times than the optical breaks. However, this model requires a long-lived central engine, which may not be the case with most of the GRBs.

5.2. An Emerging Class of Hyper-Energetic ($E > 10^{52} \text{ erg}$) GRBs?

With GRB 070125, we now have found three *Swift* events with total energy release in excess of 10^{52} erg : GRB 050904 (Frail et al. 2006) and GRB 050820A (Cenko et al. 2006b). While both GRB 050904 and GRB 050820A appear to have exploded in an dense circumburst medium, the lack of a bright radio afterglow from GRB 050820A indicates a more typical environment. Moreover, with the exception of the total energy release, other parameters derived from broadband modeling are in line with previous studies of less energetic GRBs (Panaiteescu & Kumar 2001; Yost et al. 2003b). It seems likely, therefore, that some factor intrinsic to the progenitor system is responsible for the large energy release.

At first blush, it seems surprising that *Swift* has detected three of the most energetic GRBs ever. With its increase high-energy sensitivity, *Swift* should preferentially select GRBs at the low end of the fluence distribution. We note, however, that a strong selection bias exists. As first noted by Kocevski & Butler (2007), in many *Swift* X-ray light curves, the

last XRT measurement is not sufficient to rule out a collimation-corrected prompt energy release of $\sim 10^{51}$ erg. Similarly, in the optical bandpass, Dai et al. (2007) have shown that at least some jet breaks occur at late times beyond the sensitivity of medium aperture facilities.

While a detailed discussion of the relative rates of hyper-energetic events is still premature, it is clear at this point that, at the very least, the prompt γ -ray energy distribution is significantly broader than previously believed (Kocevski & Butler 2007). Coupled with the recent controversy surrounding the validity of the many high-energy correlations, we believe the future utility of GRBs as cosmological probes is significantly lessened.

Even more importantly, however, hyper-energetic GRBs have important consequences for progenitor models. Sustained engine activity has been seen now in many GRBs (Burrows et al. 2005b). This poses a problem for the collapsar model, as the duration of the central engine should not significantly exceed the accretion time scale onto the remnant black hole (Woosley 1993). Late-time engine activity is naturally accommodated by models in which the central object is a magnetar (Usov 1992). The existence of hyper-energetic GRBs, however, is a direct and severe challenge to the magnetar model.

With the current rate of hyper-energetic events ($\sim 1 \text{ yr}^{-1}$), coupled with the difficulty in measuring late jet breaks for more typical *Swift* events, future prospects look grim. However, the impending launch of *GLAST* offers a new hope in the study of GRB energetics. Much like blazars, those GRBs capable of producing GeV photons detectable by the Large Area Telescope should be the most energetic and narrowly beamed events. Together, synergistic *GLAST* and *Swift* observations in the coming years should be able to shed light on the opening angles and energy release of a large sample of GRBs.

5.3. The Unusual Environment of GRB 070125

Our observations presented here, particularly the bright, self-absorbed radio afterglow, indicate GRB 070125 exploded in a dense circum-burst medium. In a separate work, however, Cenko et al. (2007) have reported spectroscopic observations indicating an environment almost completely devoid of absorbing material. Cenko et al. (2007) furthermore find no evidence of an underlying host galaxy to deep ($R > 25$ mag) limits. We briefly reiterate here the resolution of this apparent paradox.

The key to understanding the environment of GRB 070125 is to note that the broadband afterglow emission and the super-posed spectroscopic absorption features derive from distinct physical regions. Afterglow emission is caused by electrons in the circum-burst medium accelerated by the outgoing blastwave (e.g. Piran 2005b). These electrons reside relatively

close to the explosion center, typically at radii $r \leq 1$ pc.

We have strong evidence, however, that the absorption features seen super-posed on GRB afterglow spectra derive from material at significantly larger distances from the explosion site: $r \approx 1$ kpc, or within the host galaxy ISM. Evidence in support of this large distance comes primarily from two lines of argument. First, the presence of Mg I indicates a large distance from the explosion site, as the first ionization energy of Mg falls below 1 Ryd, and thus any Mg near the GRB would be ionized to at least Mg II (Prochaska et al. 2007). Second, Vreeswijk et al. (2007) have reported the detection of variability in the fine structure levels of Fe II from UV pumping for GRB 060418. By modeling the variability over time, they were able to measure the GRB-absorber distance: $d = 1.7 \pm 0.2$ kpc.

While this explains the apparent density paradox, we are still left to explain how a dense circum-burst medium could be embedded in such a tenuous ISM. Taking a clue from the lack of an underlying host detection, we suggested GRB 070125 may have exploded in a dense stellar cluster enriched by galaxy interactions. Star formation in such extreme environments can be seen in the local universe (e.g. Tadpole galaxy; Jarrett et al. 2006), and under our hierarchical picture of galaxy formation, such interactions should have occurred more frequently at $z > 1$. The report of the detection of a faint source at the afterglow location at late times (Dai et al. 2007) may call this interpretation into question, although it is unclear whether this emission is attributable to the fading afterglow or an underlying host (or some combination thereof). Regardless, future high-resolution imaging (i.e. *HST*) seems worthwhile to pin down the environment of this truly unique event.

5.4. Early radio emission by the reverse shock?

GRB 070125 was not detected at $t \sim 1.5$ d with the WSRT, and then was detected by both the VLA and the WSRT around day 5. It remained below detection level for the next 15 days, before rebrightening on day 22. We explore the possibility that the flux from the GRB at $t \sim 5$ d could be emission from a reverse shock. We first consider the possibility that the non-detection was caused by modulations due to scintillation.

The modulation in flux density due to the refractive scintillation can decrease the flux density at the most up to $\Delta f_\nu \sim 100 \mu\text{Jy}$. To check for this possibility, we combined all the eight observations taken during the 15 day non-detection phase. This vastly improved the signal-to-noise ratio. The flux density we obtained at the GRB position is $70 \pm 25 \mu\text{Jy}$, much lower than scintillation can explain.

According to the internal-external shock model for GRBs, the prompt emission is pro-

duced by internal shocks within a relativistic outflow, while the afterglow is produced by external shocks with the interstellar medium. The reverse shock has a much lower temperature than that of the forward shock so it radiates at considerably lower frequencies. In this scenario using the ISM model, the reverse shock emission peaks in the optical band at (Nakar & Piran 2005):

$$t_o = \max(\Delta/c, t_{\text{dec}}).$$

For GRB 070125 we calculate $t_o \approx 30$ sec. This corresponds to the time of peak in the radio band to be:

$$t_{\text{radio}} = \frac{\nu_a^r t_o}{\nu_{\text{radio}}}$$

Here ν_a^r is the synchrotron self-absorption frequency, which can be written as (Nakar & Piran 2005):

$$\nu_a^r(t_0) = 6 \times 10^{12} \text{ Hz} [(1+z)^{-(p+6)/8} \epsilon_{e,-1}^{p-1} \epsilon_{B,-2}^{(p+2)/4} (n E_{54})^{(p+6)/8} t_{o,2}^{-(3p+10)/8}]^{2/(p+4)}.$$

For values obtained from our multiwavelength analysis, we calculate $\nu_a^r = 3 \times 10^{13}$ Hz and $t_{\text{radio}} \approx 2.25$ days. Hence, the reverse shock emission peaks in the radio bands around $t \sim 2$ d. We now estimate the peak radio flux density for the reverse shock. This can be written as:

$$\frac{F_{\text{radio}}^r}{F_o^r} \left(\frac{t_{\text{radio}}}{t_o} \right)^{(p-1)/2+1.3} = \left(\frac{\nu_{\text{opt}}}{\nu_{\text{radio}}} \right)^{(p-1)/2},$$

where F_o is the peak optical flux density expressed as (Nakar & Piran 2005):

$$F_o^r \sim 16.6 \text{ mJy} (1+z)^{-(4+p)/8} n^{(p+2)/8} E_{52}^{(p+8)/8} \left(\frac{\epsilon_e}{0.1} \right)^{p-1} \left(\frac{\epsilon_B}{0.01} \right)^{(p+1)/4} \left(\frac{t_o}{100 \text{ s}} \right)^{-3p/8} D_{28}^{-2}$$

For our best fit parameters, this value is ~ 1 mJy, which gives the peak radio flux density to be $\sim 1 \mu\text{Jy}$, which is two orders on magnitude than the observed one. This shows that a reverse shock is not strong enough to explain the detection on day 5. We cannot explain this strange behavior.

5.5. GRB with high radiative efficiency?

One of the major concerns for GRB 070125 is the difference between the isotropic γ -ray energy obtained from the high-energy fluence and the isotropic-equivalent blastwave energy obtained from our best fit model on the day when $\nu_c = \nu_m$. The isotropic-equivalent kinetic energy is an order of magnitude smaller than the isotropic γ -ray energy (10^{54} erg, §3.3). However, at very early times, the afterglow is in the fast cooling regime, where it

undergoes significant loss of the energy because it is highly radiative. The fireball may lose as much as 80% of its energy during this phase (Harrison et al. 2001; Cohen et al. 1998). If we incorporate radiative corrections, we may derive a more accurate estimate of the actual isotropic blastwave energy. From Wu et al. (2005); Sari (1997) we find:

$$E(t) = E_0 \left(\frac{t}{t_0} \right)^{-\frac{17\epsilon_e}{12}}$$

for the ISM model and

$$E(t) = E_0 \left(\frac{t}{t_0} \right)^{-\frac{3\epsilon_e}{2}}$$

for the wind model. For the broadband modeling parameters, the isotropic kinetic energy one hour after the explosion is $(5.04 \pm 0.87) \times 10^{53}$ and $(3.88 \pm 3.11) \times 10^{55}$ erg for the ISM and the wind models, respectively. Here, the energy for the wind model is rather unphysical. The efficiency η_γ for the ISM model is 0.67.

5.6. Wind model vs ISM model

In terms of reduced χ^2 for best fit, wind model is slightly better. However, the wind model requires an electron energy density fraction close to 1, which is very unlikely. The best fit parameters in the wind model are rather unphysical, with less constrained boundaries. However, fixing the electron energy fraction to be 0.4 also gives reasonable fits. Evidence favoring the ISM model comes from the fireball size estimation from the scintillation data. However, the uncertainties in the diffraction scintillation time estimates may bring large uncertainties in the size estimates. Based on the energetics arguments stated above, the ISM model is favored over the wind model, but we can by no means definitely dismiss the latter.

6. Conclusion

GRB 070125 is one of the brightest GRBs ever detected, both in terms of its prompt high-energy fluence and its optical and radio afterglows. The isotropic equivalent energy for the GRB is 10^{54} erg. This is the most extensively followed GRB in multiwavebands in the *Swift* era. The richness of the data allowed us to derive many important properties of the GRB and place useful constraints on many parameters. GRB 070125 was one of the few GRBs with sub-mm observations at various epochs. Our 95 GHz and 250 GHz observations

with CARMA and IRAM, respectively, gave a robust determination of the peak flux density and ν_m , and constrained the power (νf_ν) (Fig. 6).

Simultaneous fitting to optical and X-ray data favors a jet break at day 3.78 than the single powerlaw model. The evidence for the jet break is indisputable in the optical R and i' bands with pre-break and post-break slopes being 1.73 and 2.49 respectively. However, the jet break is not very prominent in the X-ray band. When we do the independent fit to optical and X-ray bands, the optical best fit is consistent with our joint fit. However, the jet break in the X-ray band is shifted to day ~ 10 . Using the best fit parameters of the model, we show that the inverse Compton effects will dominate throughout our observations with pronounced effects in X-ray frequencies. These effects delay the jet break in the X-ray band.

We had long observations of the GRB at three epochs in the 8 GHz band. These data gave evidence for diffractive scintillations, which gave an upper limit on the size of the fireball after the jet break, until the Sedov-Taylor phase started. This estimate of the fireball size is consistent with the one obtained from the broadband modeling in a constant density medium.

We obtained synchrotron self absorption frequency estimates at various epochs from the VLA radio data. The evolution of the synchrotron self absorption frequency is $t^{-0.24 \pm 0.05}$, which is consistent with the one expected ($t^{-0.2}$) in the standard afterglow model. Synchrotron self absorption frequency estimates indicate that the GRB afterglow is moving in a dense medium.

Our model fits could not distinguish between the ISM density profile and the wind-like density profile. The χ^2 fits were marginally better for the wind model but it needed an unphysically high electron energy fraction (~ 1). When we fixed the electron energy density fraction to 0.4 in the wind model, it did give decent fits and physical parameter values. However, the parameter values in the ISM model are more robust and change little with little change in the input values, unlike the wind model which is rather unstable. In both the ISM and the wind models, the radiative efficiency of the GRB is very high ($> 60\%$).

We suggest that IC scattering is a potential candidate in flattening the light curve and delay the jet break in other *Swift* events and explain the absence of a jet break in X-ray light curves of some of the *Swift* bursts.

Even though GRB 070125 has rich multiwaveband data, we could not nail down some of the lingering issues, such as Wind vs ISM density profile. One reason for this is that much of the evolution is in the jet break phase, when the ISM and Wind models have similar properties. Very dense samples of sensitive radio, X-ray, γ -ray and optical data from the very beginning until the GRB fades below the detection limit are needed. In the future, a

combination of *Swift* GLAST, ALMA, EVLA, and various optical telescopes will provide this opportunity.

PC thanks the VLA staff for making radio observations, without which this work was not possible. PC is a Jansky fellow at National Radio Astronomy Observatory. The National Radio Astronomy Observatory is a facility of the National Science Foundation operated under cooperative agreement by Associated Universities, Inc. We thank Sarah Yost for providing us the GRB broadband modeling code and helping out in running the code. PC used the fussy calculator (<http://fussy.googlecode.com>) for error propagation calculations and wish to thank its author, Sanjay Bhantagar. RAC was supported in part by NASA grant NNG06GJ33G.

REFERENCES

Adelman-McCarthy, J. K. et al. 2007, arXiv:astro-ph/0707.3413

Amati, L. 2006, preprint (astro-ph/0601553)

Band, D., Matteson, J., Ford, L., Schaefer, B., Palmer, D., Teegarden, B., Cline, T., Briggs, M., Paciesas, W., Pendleton, G., Fishman, G., Kouveliotou, C., Meegan, C., Wilson, R., & Lestrade, P. 1993, ApJ, 413, 281

Bellm, E. C., Hurley, K., Pal'shin, V., Yamaoka, K., Bandstra, M. E., Boggs, S. E., Hong, S., Kodaka, N., Kozyrev, A. S., Litvak, M. L., Mitrofanov, I. G., Nakagawa, Y. E., Ohno, M., Onda, K., Sanin, A. B., Sugita, S., Tashiro, M., Tretyakov, V. I., Urata, Y., & Wigger, C. 2007, ArXiv e-prints, 710

Berger, E., Kulkarni, S. R., & Frail, D. A. 2003a, ApJ, 590, 379

—. 2004, ApJ, 612, 966

Berger, E., Kulkarni, S. R., Pooley, G., Frail, D. A., McIntyre, V., Wark, R. M., Sari, R., Soderberg, A. M., Fox, D. W., Yost, S., & Price, P. A. 2003b, Nature, 426, 154

Burrows, D. N., Hill, J. E., Nousek, J. A., Kennea, J. A., Wells, A., Osborne, J. P., Abbey, A. F., Beardmore, A., Mukerjee, K., Short, A. D. T., Chincarini, G., Campana, S., Citterio, O., Moretti, A., Pagani, C., Tagliaferri, G., Giommi, P., Capalbi, M., Tamburelli, F., Angelini, L., Cusumano, G., Bräuninger, H. W., Burkert, W., & Hartner, G. D. 2005a, Space Science Reviews, 120, 165

Burrows, D. N. & Racusin, J. 2007a, GRB Coordinates Network, 6181, 1

—. 2007b, ArXiv Astrophysics e-prints, astro-ph/0702633

Burrows, D. N., Romano, P., Falcone, A., Kobayashi, S., Zhang, B., Moretti, A., O'Brien, P. T., Goad, M. R., Campana, S., Page, K. L., Angelini, L., Barthelmy, S., Beardmore, A. P., Capalbi, M., Chincarini, G., Cummings, J., Cusumano, G., Fox, D., Giommi, P., Hill, J. E., Kennea, J. A., Krimm, H., Mangano, V., Marshall, F., Mészáros, P., Morris, D. C., Nousek, J. A., Osborne, J. P., Pagani, C., Perri, M., Tagliaferri, G., Wells, A. A., Woosley, S., & Gehrels, N. 2005b, Science, 309, 1833

Cenko, S. B. & Fox, D. B. 2007, GRB Coordinates Network, 6028, 1

Cenko, S. B., Fox, D. B., Moon, D.-S., Harrison, F. A., Kulkarni, S. R., Henning, J. R., Guzman, C. D., Bonati, M., Smith, R. M., Thicksten, R. P., Doyle, M. W., Petrie, H. L., Gal-Yam, A., Soderberg, A. M., Anagnostou, N. L., & Laity, A. C. 2006a, PASP, 118, 1396

Cenko, S. B., Kasliwal, M., Harrison, F. A., Pal'shin, V., Frail, D. A., Cameron, P. B., Berger, E., Fox, D. B., Gal-Yam, A., Kulkarni, S. R., Moon, D.-S., Nakar, E., Ofek, E. O., Penprase, B. E., Price, P. A., Sari, R., Schmidt, B. P., Soderberg, A. M., Aptekar, R., Frederiks, D., Golenetskii, S., Burrows, D. N., Chevalier, R. A., Gehrels, N., McCarthy, P. J., Nousek, J. A., & Piran, T. 2006b, ApJ, 652, 490

Cenko, S. B. et al. 2007, ApJ, submitted

Chandra, P., Chandra, I., & Gupta, N. 2007, GRB Coordinates Network, 6102, 1

Chandra, P. & Frail, D. A. 2007, GRB Coordinates Network, 6061, 1

Cohen, E., Piran, T., & Sari, R. 1998, ApJ, 509, 717

Cordes, J. M. & Lazio, T. J. W. 2002, ArXiv Astrophysics e-prints

Corsi, A. & Piro, L. 2006, A&A, 458, 741

Dai, X., Garnavich, P. M., Prieto, J. L., Stanek, K. Z., Kochanek, C. S., Bechtold, J., Bouche, N., Buschkamp, P., Diolaiti, E., Fan, X., Giallongo, E., Gredel, R., Hill, J. M., Jiang, L., McClelland, C., Milne, P., Pedichini, F., Pogge, R. W., Ragazzoni, R., Rhoads, J., Smareglia, R., Thompson, D., & Wagner, R. M. 2007, ArXiv e-prints, 712

Dickey, J. M. & Lockman, F. J. 1990, ARA&A, 28, 215

Evans, P. A., Beardmore, A. P., Page, K. L., Tyler, L. G., Osborne, J. P., Goad, M. R., O'Brien, P. T., Vetere, L., Racusin, J., Morris, D., Burrows, D. N., Capalbi, M., Perri, M., Gehrels, N., & Romano, P. 2007, *A&A*, 469, 379

Frail, D. A., Cameron, P. B., Kasliwal, M., Nakar, E., Price, P. A., Berger, E., Gal-Yam, A., Kulkarni, S. R., Fox, D. B., Soderberg, A. M., Schmidt, B. P., Ofek, E., & Cenko, S. B. 2006, *ApJ*, 646, L99

Frail, D. A., Kulkarni, S. R., Sari, R., Djorgovski, S. G., Bloom, J. S., Galama, T. J., Reichart, D. E., Berger, E., Harrison, F. A., Price, P. A., Yost, S. A., Diercks, A., Goodrich, R. W., & Chaffee, F. 2001, *ApJ*, 562, L55

Frail, D. A., Soderberg, A. M., Kulkarni, S. R., Berger, E., Yost, S., Fox, D. W., & Harrison, F. A. 2005, *ApJ*, 619, 994

Frail, D. A., Waxman, E., & Kulkarni, S. R. 2000, *ApJ*, 537, 191

Frail, D. A., Yost, S. A., Berger, E., Harrison, F. A., Sari, R., Kulkarni, S. R., Taylor, G. B., Bloom, J. S., Fox, D. W., Moriarty-Schieven, G. H., & Price, P. A. 2003, *ApJ*, 590, 992

Freedman, D. L. & Waxman, E. 2001, 547, 922

Fruchter, A. S., Thorsett, S. E., Metzger, M. R., Sahu, K. C., Petro, L., Livio, M., Ferguson, H., Pian, E., Hogg, D. W., Galama, T., Gull, T. R., Kouveliotou, C., Macchett, D., Van Paradijs, J., Pedersen, H., & Smette, A. 1999, 519, L13

Fukugita, M., Shimasaku, K., & Ichikawa, T. 1995, *PASP*, 107, 945

Garmire, G. P., Bautz, M. W., Ford, P. G., Nousek, J. A., & Ricker, Jr., G. R. 2003, in Presented at the Society of Photo-Optical Instrumentation Engineers (SPIE) Conference, Vol. 4851, X-Ray and Gamma-Ray Telescopes and Instruments for Astronomy. Edited by Joachim E. Truemper, Harvey D. Tananbaum. Proceedings of the SPIE, Volume 4851, pp. 28-44 (2003)., ed. J. E. Truemper & H. D. Tananbaum, 28-44

Garnavich, P., Fan, X., Jiang, L., Dai, X., Kuhn, O., Bouche, N., Buschkamp, P., Smith, P., Milne, P., Bechtold, J., Stanek, K. Z., Prieto, J., Wagner, R. M., Rhoads, J., Hill, J., Baruffolo, A., Desantis, C., Diolaiti, E., Dipaola, A., Farinato, J., Fontana, A., Gallozzi, S., Gasparo, F., Giallongo, E., Grazian, A., Pasian, F., Pedichini, F., Ragazzoni, R., Smareglia, R., Speziali, R., Testa, V., & Vernet, E. 2007, GRB Coordinates Network, 6165, 1

Golenetskii, S., Aptekar, R., Mazets, E., Pal'Shin, V., Frederiks, D., & Cline, T. 2007, GRB Coordinates Network, 6049, 1

Goodman, J. 1997, New Astronomy, 2, 449

Harrison, F. A., Bloom, J. S., Frail, D. A., Sari, R., Kulkarni, S. R., Djorgovski, S. G., Axelrod, T., Mould, J., Schmidt, B. P., Wieringa, M. H., Wark, R. M., Subrahmanyan, R., McConnell, D., McCarthy, P. J., Schaefer, B. E., McMahon, R. G., Markze, R. O., Firth, E., Soffitta, P., & Amati, L. 1999, 523, L121

Harrison, F. A., Yost, S. A., Sari, R., Berger, E., Galama, T. J., Holtzman, J., Axelrod, T., Bloom, J. S., Chevalier, R., Costa, E., Diercks, A., Djorgovski, S. G., Frail, D. A., Frontera, F., Hurley, K., Kulkarni, S. R., McCarthy, P., Piro, L., Pooley, G. G., Price, P. A., Reichart, D., Ricker, G. R., Shepherd, D., Schmidt, B., Walter, F., & Wheeler, C. 2001, ApJ, 559, 123

Hook, I., Allington-Smith, J. R., Beard, S. M., Crampton, D., Davies, R. L., Dickson, C. G., Ebbers, A. W., Fletcher, J. M., Jorgensen, I., Jean, I., Juneau, S., Murowinski, R. G., Nolan, R., Laidlaw, K., Leckie, B., Marshall, G. E., Purkins, T., Richardson, I. M., Roberts, S. C., Simons, D. A., Smith, M. J., Stilburn, J. R., Szeto, K., Tierney, C., Wolff, R. J., & Wooff, R. 2003, in Instrument Design and Performance for Optical/Infrared Ground-based Telescopes. Edited by Iye, Masanori; Moorwood, Alan F. M. Proceedings of the SPIE, Volume 4841, pp. 1645-1656 (2003)., ed. M. Iye & A. F. M. Moorwood, 1645–1656

Hurley, K., Cline, T., Mitrofanov, I., Kozyrev, A., Litvak, M., Sanin, A., Tret'yakov, V., Parshukov, A., Boynton, W., Fellows, C., Harshman, K., Shinohara, C., Starr, R., Yamaoka, K., Ohno, M., Fukazawa, Y., Takahashi, T., Tashiro, M., Terada, Y., Murakami, T., Makishima, K., Smith, D. M., Lin, R. P., McTiernan, J., Schwartz, R., Wigger, C., Hajdas, W., Zehnder, A., von Kienlin, A., Lichti, G., Rau, A., Cummings, J., Krimm, H., Barthelmy, S., & Gehrels, N. 2007, GRB Coordinates Network, 6024, 1

Jarrett, T. H., Polletta, M., Fournon, I. P., Stacey, G., Xu, K., Siana, B., Farrah, D., Berta, S., Hatziminaoglou, E., Rodighiero, G., Surace, J., Domingue, D., Shupe, D., Fang, F., Lonsdale, C., Oliver, S., Rowan-Robinson, M., Smith, G., Babbedge, T., Gonzalez-Solares, E., Masci, F., Franceschini, A., & Padgett, D. 2006, AJ, 131, 261

Jordi, K., Grebel, E. K., & Ammon, K. 2006, A&A, 460, 339

Kocevski, D. & Butler, N. 2007, astro-ph/0707.4478

Kulkarni, S. R., Djorgovski, S. G., Odewahn, S. C., Bloom, J. S., Gal, R. R., Koresko, C. D., Harrison, F. A., Lubin, L. M., Armus, L., Sari, R., Illingworth, G. D., Kelson, D. D., Magee, D. K., Dokkum, P. G. V., Frail, D. A., Mulchaey, J. S., Malkan, M. A., McClean, I. S., Teplitz, H. I., Koerner, D., Kirkpatrick, D., Kobayashi, N., Yadigaroglu, I.-A., Halpern, J., Piran, T., Goodrich, R. W., Chaffee, F. H., Feroci, M., & Costa, E. 1999, *Nature*, 398, 389

Kumar, P. 2000, 538, L125

Li, Z.-Y. & Chevalier, R. A. 2003, in *Lecture Notes in Physics*, Berlin Springer Verlag, Vol. 598, *Supernovae and Gamma-Ray Bursters*, ed. K. Weiler, 419–444

Meszaros, P. 2006, *Reports of Progress in Physics*, 69, 2259

Nakar, E. & Piran, T. 2005, *ApJ*, 619, L147

Oke, J. B., Cohen, J. G., Carr, M., Cromer, J., Dingizian, A., Harris, F. H., Labrecque, S., Lucinio, R., Schaal, W., Epps, H., & Miller, J. 1995, *PASP*, 107, 375

Panaitescu, A. 2007, ArXiv e-prints, 708

Panaitescu, A. & Kumar, P. 2001, 560, L49

Pei, Y. C. 1992, *ApJ*, 395, 130

Piran, T. 1999, *Phys. Rep.*, 314, 575

—. 2005a, *Reviews of Modern Physics*, 76, 1143

—. 2005b, *Reviews of Modern Physics*, 76, 1143

Prochaska, J. X., Chen, H.-W., Dessauges-Zavadsky, M., & Bloom, J. S. 2007, arXiv:astro-ph/0703665

Racusin, J. & Vetere, L. 2007, *GRB Coordinates Network*, 6030, 1

Rhoads, J. E. 1999, *ApJ*, 525, 737

Sari, R. 1997, *ApJ*, 489, L37+

Sari, R. & Esin, A. A. 2001, *ApJ*, 548, 787

Sari, R., Piran, T., & Halpern, J. P. 1999, 519, L17

Sari, R., Piran, T., & Narayan, R. 1998, 497, L17

Sault, R. J., Teuben, P. J., & Wright, M. C. H. 1995, in Astronomical Society of the Pacific Conference Series, Vol. 77, Astronomical Data Analysis Software and Systems IV, ed. R. A. Shaw, H. E. Payne, & J. J. E. Hayes, 433–+

Schlegel, D. J., Finkbeiner, D. P., & Davis, M. 1998, *ApJ*, 500, 525

Stanek, K. Z., Garnavich, P. M., Kaluzny, J., Pych, W., & Thompson, I. 1999, 522, L39

Usov, V. V. 1992, *Nature*, 357, 472

van der Horst, A. J. 2007, GRB Coordinates Network, 6042, 1

Vreeswijk, P. M., Ledoux, C., Smette, A., Ellison, S. L., Jaunsen, A. O., Andersen, M. I., Fruchter, A. S., Fynbo, J. P. U., Hjorth, J., Kaufer, A., Møller, P., Petitjean, P., Savaglio, S., & Wijers, R. A. M. J. 2007, *A&A*, 468, 83

Walker, M. A. 1998, *MNRAS*, 294, 307

—. 2001, *MNRAS*, 321, 176

Wei, D. M. & Lu, T. 1998, *ApJ*, 505, 252

—. 2000, *A&A*, 360, L13

Woosley, S. E. 1993, *ApJ*, 405, 273

Wu, X. F., Dai, Z. G., Huang, Y. F., & Lu, T. 2005, *ApJ*, 619, 968

Yost, S. A. 2004, PhD thesis, AA(CALIFORNIA INSTITUTE OF TECHNOLOGY)

Yost, S. A., Harrison, F. A., Sari, R., & Frail, D. A. 2003a, *ApJ*, 597, 459

—. 2003b, *ApJ*, 597, 459

Zhang, B., Fan, Y. Z., Dyks, J., Kobayashi, S., Mészáros, P., Burrows, D. N., Nousek, J. A., & Gehrels, N. 2006, *ApJ*, 642, 354

Table 1. X-ray observations of the GRB 070125 with *Swift* at 3.594×10^{17} Hz

Days since Explosion	Counts/s (0.3-10.0 keV)	Flux (0.3-10.0 keV) erg s ⁻¹ cm ⁻²	Flux Density μJy
0.54203	0.064175 ± 0.016806	$3.00 \times 10^{-12} \pm 7.85 \times 10^{-13}$	0.240 ± 0.063
0.544683	0.096087 ± 0.025044	$4.49 \times 10^{-12} \pm 1.17 \times 10^{-12}$	0.360 ± 0.094
0.546296	0.104163 ± 0.027022	$4.86 \times 10^{-12} \pm 1.26 \times 10^{-12}$	0.390 ± 0.10
0.548676	0.060351 ± 0.015879	$2.82 \times 10^{-12} \pm 7.41 \times 10^{-13}$	0.226 ± 0.059
0.552346	0.065485 ± 0.017149	$3.06 \times 10^{-12} \pm 8.01 \times 10^{-13}$	0.245 ± 0.064
0.554473	0.106140 ± 0.023902	$4.96 \times 10^{-12} \pm 1.12 \times 10^{-12}$	0.398 ± 0.089
0.55787	0.098574 ± 0.017867	$4.60 \times 10^{-12} \pm 8.34 \times 10^{-13}$	0.369 ± 0.067
0.607229	0.083110 ± 0.021560	$3.88 \times 10^{-12} \pm 1.01 \times 10^{-12}$	0.311 ± 0.081
0.609911	0.062137 ± 0.016195	$2.90 \times 10^{-12} \pm 7.56 \times 10^{-13}$	0.233 ± 0.061
0.612569	0.084761 ± 0.022197	$3.96 \times 10^{-12} \pm 1.04 \times 10^{-12}$	0.317 ± 0.083
0.615869	0.056149 ± 0.014844	$2.62 \times 10^{-12} \pm 6.93 \times 10^{-13}$	0.210 ± 0.056
0.619209	0.065275 ± 0.017013	$3.05 \times 10^{-12} \pm 7.94 \times 10^{-13}$	0.245 ± 0.063
0.623267	0.051077 ± 0.010302	$2.39 \times 10^{-12} \pm 4.81 \times 10^{-13}$	0.191 ± 0.038
0.675751	0.077789 ± 0.020564	$3.63 \times 10^{-12} \pm 9.60 \times 10^{-13}$	0.291 ± 0.077
0.678452	0.057316 ± 0.015010	$2.68 \times 10^{-12} \pm 7.01 \times 10^{-13}$	0.215 ± 0.056
0.682168	0.062115 ± 0.016114	$2.90 \times 10^{-12} \pm 7.52 \times 10^{-13}$	0.233 ± 0.060
0.685654	0.055467 ± 0.014663	$2.59 \times 10^{-12} \pm 6.85 \times 10^{-13}$	0.208 ± 0.055
0.688978	0.062736 ± 0.016507	$2.93 \times 10^{-12} \pm 7.71 \times 10^{-13}$	0.235 ± 0.062
0.692052	0.067433 ± 0.017235	$3.15 \times 10^{-12} \pm 8.05 \times 10^{-13}$	0.253 ± 0.064
0.733542	0.081260 ± 0.021280	$3.79 \times 10^{-12} \pm 9.94 \times 10^{-13}$	0.304 ± 0.079
0.737868	0.071125 ± 0.013240	$3.32 \times 10^{-12} \pm 6.18 \times 10^{-13}$	0.266 ± 0.049
1.34534	0.032554 ± 0.007425	$1.52 \times 10^{-12} \pm 3.47 \times 10^{-13}$	0.122 ± 0.028
1.35747	0.041983 ± 0.008103	$1.96 \times 10^{-12} \pm 3.78 \times 10^{-13}$	0.157 ± 0.030
1.41052	0.027726 ± 0.006362	$1.29 \times 10^{-12} \pm 2.97 \times 10^{-13}$	0.104 ± 0.023
1.42675	0.039339 ± 0.009101	$1.84 \times 10^{-12} \pm 4.25 \times 10^{-13}$	0.147 ± 0.034
1.47713	0.032748 ± 0.007624	$1.53 \times 10^{-12} \pm 3.56 \times 10^{-13}$	0.123 ± 0.028
1.48861	0.038279 ± 0.007576	$1.79 \times 10^{-12} \pm 3.54 \times 10^{-13}$	0.143 ± 0.028
1.78359	0.014033 ± 0.002725	$6.55 \times 10^{-13} \pm 1.27 \times 10^{-13}$	0.053 ± 0.010
1.8904	0.013734 ± 0.003671	$6.41 \times 10^{-13} \pm 1.71 \times 10^{-13}$	0.051 ± 0.014
1.94946	0.015608 ± 0.004296	$7.29 \times 10^{-13} \pm 2.01 \times 10^{-13}$	0.058 ± 0.016
2.05462	0.012729 ± 0.002489	$5.94 \times 10^{-13} \pm 1.16 \times 10^{-13}$	0.048 ± 0.009
2.1865	0.009233 ± 0.002318	$4.31 \times 10^{-13} \pm 1.08 \times 10^{-13}$	0.035 ± 0.009
2.30888	0.010806 ± 0.002868	$5.04 \times 10^{-13} \pm 1.34 \times 10^{-13}$	0.040 ± 0.011
2.47372	0.015085 ± 0.003520	$7.04 \times 10^{-13} \pm 1.64 \times 10^{-13}$	0.057 ± 0.013
2.68019	0.006752 ± 0.001515	$3.15 \times 10^{-13} \pm 7.07 \times 10^{-14}$	0.025 ± 0.006
2.83975	0.010154 ± 0.002670	$4.74 \times 10^{-13} \pm 1.25 \times 10^{-13}$	0.038 ± 0.010

Table 1—Continued

Days since Explosion	Counts/s (0.3-10.0 keV)	Flux (0.3-10.0 keV) erg s ⁻¹ cm ⁻²	Flux Density μJy
3.07971	0.007542 ± 0.001640	$3.52 \times 10^{-13} \pm 7.66 \times 10^{-14}$	0.028 ± 0.006
3.3886	0.005554 ± 0.001293	$2.59 \times 10^{-13} \pm 6.04 \times 10^{-14}$	0.021 ± 0.0048
3.59126	0.006728 ± 0.001769	$3.14 \times 10^{-13} \pm 8.26 \times 10^{-14}$	0.025 ± 0.007
4.04549	0.004496 ± 0.001265	$2.10 \times 10^{-13} \pm 5.91 \times 10^{-14}$	0.017 ± 0.0056
5.97272	0.001798 ± 0.000493	$8.40 \times 10^{-14} \pm 2.30 \times 10^{-14}$	0.007 ± 0.0018
9.08277	0.001052 ± 0.000293	$4.91 \times 10^{-14} \pm 1.36 \times 10^{-14}$	0.004 ± 0.001
10.5438	0.000785 ± 0.000239	$3.67 \times 10^{-14} \pm 1.11 \times 10^{-14}$	0.003 ± 0.001
14.562	< 0.000277	< 1.29×10^{-14}	< 0.001
39.6190	< 0.000167	< 2×10^{-15}	< 0.0002 ^a

^a *Chandra* observations, GCN 6186

Table 2. Optical/IR/UV observations of the GRB 070125

Days since Explosion	Filter	λ in μm	F_0 Jy	Magnitude	A_λ mag	Corrected mag	Flux density μJy	Reference ^a
0.54034	V	0.55	3590	18.54 ± 0.06	0.17	18.37	161.1 ± 8.8	GCN6041, 6036
0.55035	B	0.45	4020	18.92 ± 0.03	0.23	18.69	134.3 ± 3.8	GCN6036, 6041
0.67441	V	0.55	3590	18.74 ± 0.07	0.17	18.57	134.0 ± 8.5	GCN6036, 6041
0.68433	B	0.45	4020	19.03 ± 0.06	0.23	18.80	121.4 ± 6.9	GCN6036, 6041
0.79149	R	0.66	3020	18.59 ± 0.03	0.14	18.45	125.9 ± 3.9	P60
0.79379	R	0.66	3020	18.51 ± 0.03	0.14	18.37	135.6 ± 4.3	P60
0.79609	R	0.66	3020	18.57 ± 0.03	0.14	18.43	128.2 ± 4.1	P60
0.79848	R	0.66	3020	18.61 ± 0.03	0.14	18.47	123.7 ± 3.7	P60
0.80087	R	0.66	3020	18.53 ± 0.05	0.14	18.39	133.1 ± 6.6	P60
0.80229	R	0.66	3020	$18.60 \pm -$	0.14	18.46	$124.8 \pm -$	GCN6028
0.80326	R	0.66	3020	18.55 ± 0.03	0.14	18.41	130.7 ± 4.2	P60
0.89965	r'	0.63	3631	19.03 ± 0.09	0.14	18.89	100.9 ± 1.2	GMOS
0.90833	R	0.66	3020	$18.80 \pm -$	0.14	18.66	$103.7 \pm -$	GCN6044
1.08990	R	0.66	3020	18.70 ± 0.06	0.14	18.56	113.8 ± 6.5	P60
1.09277	R	0.66	3020	18.63 ± 0.07	0.14	18.49	121.3 ± 7.4	P60
1.09564	R	0.66	3020	18.69 ± 0.03	0.14	18.55	114.8 ± 3.5	P60
1.10146	R	0.66	3020	18.66 ± 0.04	0.14	18.52	118.1 ± 4.0	P60
1.10450	i'	0.77	3631	18.61 ± 0.03	0.10	18.51	143.2 ± 4.5	P60
1.10742	i'	0.77	3631	18.61 ± 0.03	0.10	18.51	143.2 ± 4.3	P60
1.11337	i'	0.77	3631	18.53 ± 0.03	0.10	18.43	154.2 ± 4.8	P60
1.11630	i'	0.77	3631	18.59 ± 0.03	0.10	18.49	146.0 ± 4.6	P60
1.11929	R	0.66	3020	18.60 ± 0.03	0.14	18.46	124.8 ± 3.6	P60
1.12222	R	0.66	3020	18.60 ± 0.03	0.14	18.46	124.8 ± 4.0	P60
1.12516	R	0.66	3020	18.64 ± 0.04	0.14	18.50	120.2 ± 4.1	P60
1.12811	R	0.66	3020	18.60 ± 0.03	0.14	18.46	124.8 ± 3.6	P60
1.13108	R	0.66	3020	18.62 ± 0.03	0.14	18.48	122.4 ± 3.6	P60
1.13405	i'	0.77	3631	18.64 ± 0.04	0.10	18.54	139.3 ± 4.8	P60
1.13698	i'	0.77	3631	18.62 ± 0.04	0.10	18.52	141.9 ± 5.1	P60
1.14743	R	0.66	3020	18.73 ± 0.15	0.14	18.59	110.6 ± 14.6	GCN6035
1.15466	R	0.66	3020	18.63 ± 0.04	0.14	18.49	121.3 ± 4.6	P60
1.15705	R	0.66	3020	18.64 ± 0.03	0.14	18.50	120.2 ± 3.6	P60
1.16182	R	0.66	3020	18.63 ± 0.03	0.14	18.49	121.3 ± 3.9	P60
1.16421	R	0.66	3020	18.66 ± 0.03	0.14	18.52	118.1 ± 3.8	P60
1.16661	i'	0.77	3631	18.65 ± 0.04	0.10	18.55	138.0 ± 4.9	P60
1.16900	i'	0.77	3631	18.64 ± 0.03	0.10	18.54	139.3 ± 4.3	P60
1.17378	i'	0.77	3631	18.66 ± 0.04	0.10	18.56	136.9 ± 4.8	P60
1.17617	i'	0.77	3631	18.68 ± 0.03	0.10	18.58	134.2 ± 4.1	P60
1.17857	R	0.66	3020	18.65 ± 0.04	0.14	18.51	119.2 ± 3.9	P60
1.18096	R	0.66	3020	18.66 ± 0.04	0.14	18.52	118.1 ± 3.9	P60
1.18336	R	0.66	3020	18.64 ± 0.04	0.14	18.50	120.2 ± 3.9	P60
1.18576	R	0.66	3020	18.72 ± 0.04	0.14	18.58	111.7 ± 3.9	P60
1.18815	R	0.66	3020	18.66 ± 0.05	0.14	18.52	118.1 ± 5.5	P60
1.19060	i'	0.77	3631	18.71 ± 0.04	0.10	18.61	130.6 ± 4.6	P60
1.19300	i'	0.77	3631	18.69 ± 0.04	0.10	18.59	133.1 ± 4.5	P60
1.19539	i'	0.77	3631	18.67 ± 0.04	0.10	18.57	135.6 ± 4.8	P60

Table 2—Continued

Days since Explosion	Filter	λ in μm	F_0 Jy	Magnitude	A_λ mag	Corrected mag	Flux density μJy	Reference ^a
1.20019	i'	0.77	3631	18.70 \pm 0.04	0.10	18.60	131.8 \pm 4.9	P60
1.20261	R	0.66	3020	18.67 \pm 0.05	0.14	18.53	116.9 \pm 5.3	P60
1.20500	R	0.66	3020	18.65 \pm 0.04	0.14	18.51	117.2 \pm 4.2	P60
1.20740	R	0.66	3020	18.65 \pm 0.09	0.14	18.51	119.2 \pm 9.7	P60
1.20980	R	0.66	3020	18.71 \pm 0.04	0.14	18.57	112.8 \pm 4.0	P60
1.21220	R	0.66	3020	18.72 \pm 0.04	0.14	18.58	111.7 \pm 4.2	P60
1.21464	i'	0.77	3631	18.71 \pm 0.05	0.10	18.61	130.6 \pm 5.5	P60
1.21704	i'	0.77	3631	18.68 \pm 0.04	0.10	18.58	134.2 \pm 5.2	P60
1.21944	i'	0.77	3631	18.71 \pm 0.04	0.10	18.61	130.6 \pm 4.9	P60
1.22185	i'	0.77	3631	18.74 \pm 0.04	0.10	18.64	127.0 \pm 4.8	P60
1.22425	i'	0.77	3631	18.67 \pm 0.04	0.10	18.57	135.6 \pm 4.8	P60
1.22521	Rc	0.66	3020	18.90 \pm 0.2	0.14	18.76	94.6 \pm 23.3	GCN6050
1.22910	R	0.66	3020	18.71 \pm 0.05	0.14	18.57	112.8 \pm 5.0	P60
1.23151	R	0.66	3020	18.70 \pm 0.09	0.14	18.56	113.8 \pm 9.3	P60
1.23391	R	0.66	3020	18.75 \pm 0.05	0.14	18.61	108.7 \pm 4.9	P60
1.23632	R	0.66	3020	18.76 \pm 0.04	0.14	18.62	107.7 \pm 4.5	P60
1.27104	Rc	0.66	3020	19.00 \pm 0.3	0.14	18.86	86.3 \pm 21.3	GCN6050
1.31410	Ic	0.81	2380	18.00 \pm 0.3	0.10	17.90	164.7 \pm 6.8	GCN6050
1.31410	g'	0.49	3631	19.60 \pm 0.2	0.06	19.54	55.4 \pm 8.6	GCN6050
1.31410	Rc	0.66	3020	18.80 \pm 0.2	0.14	18.66	103.8 \pm 17.8	GCN6050
1.35377	V	0.55	3590	19.26 \pm 0.27	0.17	19.09	83.0 \pm 18.5	GCN6041
1.37590	Rc	0.66	3020	18.70 \pm 0.2	0.14	18.56	113.8 \pm 19.5	GCN6050
1.37605	R	0.66	3020	19.09 \pm 0.05	0.14	18.95	79.6 \pm 3.7	GCN6039
1.40437	Rc	0.66	3020	19.40 \pm 0.4	0.14	19.26	59.7 \pm 18.8	GCN6050
1.79844	R	0.66	3020	19.43 \pm 0.03	0.14	19.29	58.1 \pm 1.6	P60
1.81062	i'	0.77	3631	19.49 \pm 0.03	0.10	19.39	63.7 \pm 2.0	P60
1.84702	R	0.66	3020	19.51 \pm 0.03	0.14	19.37	54.0 \pm 1.7	P60
1.85907	i'	0.77	3631	19.52 \pm 0.03	0.10	19.42	61.9 \pm 1.9	P60
1.90324	R	0.66	3020	19.59 \pm 0.03	0.14	19.45	50.1 \pm 1.3	P60
1.91542	i'	0.77	3631	19.58 \pm 0.03	0.10	19.48	58.6 \pm 1.6	P60
1.96396	Rc	0.66	3020	19.71 \pm 0.02	0.14	19.57	44.9 \pm 0.8	GCN6096
1.97868	R	0.66	3020	19.62 \pm 0.03	0.14	19.48	48.7 \pm 1.4	P60
1.99132	i'	0.77	3631	19.69 \pm 0.03	0.10	19.59	52.9 \pm 1.6	P60
2.64396	Rc	0.66	3020	20.23 \pm 0.1	0.14	20.09	27.8 \pm 2.5	GCN6047
2.65995	Rc	0.66	3020	20.26 \pm 0.11	0.14	20.12	27.0 \pm 2.7	GCN6047
2.67696	Rc	0.66	3020	20.21 \pm 0.11	0.14	20.07	28.3 \pm 2.8	GCN6047
2.78096	Rc	0.64	3020	20.25 \pm 0.11	0.14	20.11	27.3 \pm 2.7	GCN6047
2.79596	Rc	0.66	3020	20.35 \pm 0.12	0.14	20.21	24.9 \pm 2.7	GCN6047
2.81479	Ks	2.22	670	17.86 \pm 0.25	0.02	17.84	49.0 \pm 10.1	GCN6054
2.81479	J	1.26	1600	18.82 \pm 0.26	0.05	18.77	49.7 \pm 10.6	GCN6054
2.99296	R	0.66	3020	20.44 \pm 0.03	0.14	20.30	22.9 \pm 0.6	GCN6096
3.02006	R	0.66	3020	20.44 \pm 0.04	0.14	20.30	22.9 \pm 0.8	P60
3.03328	i'	0.77	3631	20.47 \pm 0.04	0.10	20.37	25.9 \pm 1.1	P60
3.62096	Rc	0.66	3020	20.80 \pm 0.2	0.14	20.66	16.4 \pm 2.8	GCN6064
3.91797	r'	0.63	3631	21.22 \pm 0.09	0.14	21.08	13.4 \pm 1.5	GMOS

Table 2—Continued

Days since Explosion	Filter	λ in μm	F_0 Jy	Magnitude	A_λ mag	Corrected mag	Flux density μJy	Reference ^a
4.03995	R	0.66	3020	21.07 ± 0.07	0.14	20.93	12.8 ± 0.8	GCN6096
4.07106	i'	0.77	3631	21.03 ± 0.10	0.10	20.93	15.5 ± 1.0	P60
4.08226	R	0.66	3020	> 20.44	0.14	> 20.30	< 22.5	P60
8.85767	R	0.66	3020	> 21.63	0.14	> 21.49	< 7.5	P60
10.0099	i'	0.77	3631	23.75 ± 0.14	0.10	23.65	1.3 ± 0.2	P60
11.82110	R	0.66	3020	> 22.57	0.14	> 22.43	< 3.2	P60
12.00096	R	0.66	3020	$23.80 \pm -$	0.14	23.66	$1.0 \pm -$	GCN6096
21.99400	R	0.66	3020	> 25.40	0.14	> 25.26	< 0.2	LRIS
21.99400	g'	0.49	3631	> 26.10	0.06	> 26.04	< 0.2	LRIS
26.79396	r	0.67	3631	26.30 ± 0.3	0.14	26.16	$0.13 \pm -$	GCN6165

Note. — P60≡ Palomer 60-inch Telescope observations.

^a• GCN 6041: *Swift* UVOT, Marshall, F.E., vanden Berk, D.E. and Racusin, J. • GCN 6036: *Swift* UVOT, Marshall, F.E., Racusin, J. • GCN 6028: Palomer 60in, Cenko, S.B. and Fox, D.B. • GCN 6044: 16in PROMPT telescope, Haislip, J., Reichart, D. and LaCluyze, A. et al. • GCN 6035: TNT 0.8m telescope, Xing, L.P., Zhai, M., Qiu, Y.L. et al. • GCN 6050: 50cm MITSuME Telescope, Yoshida, M., Yanagisawa, K., and Kawai, N., • GCN 6039: KANATA 1.5-m telescope, Uemura, M., Arai, A., and Uehara, T. • GCN 6096: MDM 2.4m and 1.3m telescopes, Mirabal, N., and Thorstensen, J.R. • GCN 6047: 152 cm Cassini Telescope, Greco, G., Terra, F., and Bartolini, C. et al. • GCN 6054: PAIRITEL 1.3m telescope, Bloom, J.S., Starr, D., and Blake, C.H. • GCN 6064: 152 cm Loiano telescope, Greco, G., Terra, F., and Bartolini, C. et al. • GCN 6165: Large Binocular Telescope, Garnavich, P., Fan, X., and Jiang, L. et al.

Table 3. Radio observations of the GRB 070125

Date of observation	Days since explosion	Telescope	Frequency in GHz	Flux density μJy	Error μJy
2007 Jan 26.82	1.51	WSRT	4.86	< 174	87
2007 Jan 29.32	4.01	VLA	8.46	360	42
2007 Jan 30.24	4.93	VLA	8.46	454	38
2007 Jan 30.95	5.64	WSRT	4.86	102	26
2007 Jan 31.07	5.76	VLA	4.86	141	58
2007 Jan 31.11	5.80	VLA	8.46	382	52
2007 Jan 31.76	6.45	GMRT	0.61	< 300	150
2007 Jan 31.83	6.52	MAMBO2	250	3140	590
2007 Feb 01.92	7.61	MAMBO2	250	1910	720
2007 Feb 02.06	7.75	VLA	8.46	563	62
2007 Feb 04.92	10.61	MAMBO2	250	< 1470	710
2007 Feb 05.03	10.72	VLA	8.46	482	52
2007 Feb 05.04	10.73	VLA	22.50	1594	70
2007 Feb 05.07	10.76	VLA	4.86	< 132	42
2007 Feb 05.29	10.98	CARMA	95	2300	700
2007 Feb 06.24	11.93	VLA	8.46	489	43
2007 Feb 06.26	11.95	VLA	4.86	< 124	34
2007 Feb 07.11	12.80	VLA	22.50	1603	235
2007 Feb 07.12	12.81	VLA	8.46	405	20
2007 Feb 07.38	13.07	VLA	14.94	1159	234
2007 Feb 08.21	13.90	VLA	14.94	917	293
2007 Feb 08.23	13.92	VLA	4.86	< 145	50
2007 Feb 08.24	13.93	VLA	8.46	559	26
2007 Feb 08.40	14.09	VLA	22.50	1621	151
2007 Feb 09.21	14.90	VLA	4.86	< 108	49
2007 Feb 09.25	14.94	VLA	8.46	399	69
2007 Feb 09.27	14.96	VLA	22.50	1343	162
2007 Feb 09.27	14.96	CARMA	95	2300	800
2007 Feb 09.28	14.97	VLA	14.94	891	129
2007 Feb 10.37	16.06	VLA	14.94	1410	137
2007 Feb 10.79	16.48	MAMBO2	250	2670	930
2007 Feb 11.08	16.77	VLA	8.46	385	42
2007 Feb 11.12	16.81	VLA	22.50	1367	104
2007 Feb 11.16	16.85	VLA	4.86	< 196	71
2007 Feb 12.08	17.77	VLA	1.46	< 920	460
2007 Feb 12.16	17.85	VLA	8.46	596	109
2007 Feb 12.20	17.89	VLA	14.94	1226	155
2007 Feb 12.21	17.90	CARMA	95	2100	700
2007 Feb 12.26	17.95	VLA	22.50	1222	167
2007 Feb 12.79	18.48	MAMBO2	250	< 1270	930
2007 Feb 13.07	18.76	VLA	1.46	< 940	600
2007 Feb 13.11	18.80	VLA	4.86	< 150	52
2007 Feb 13.17	18.86	VLA	8.46	660	39
2007 Feb 13.21	18.90	VLA	14.94	1217	197
2007 Feb 13.25	18.94	VLA	22.50	1248	83

Table 3—Continued

Date of observation	Days since explosion	Telescope	Frequency in GHz	Flux density μJy	Error μJy
2007 Feb 14.18	19.87	VLA	8.46	581	14
2007 Feb 16.17	21.86	VLA	1.46	< 1068	540
2007 Feb 16.19	21.88	VLA	4.86	< 159	47
2007 Feb 17.02	22.71	VLA	1.46	< 1152	766
2007 Feb 17.04	22.73	VLA	4.86	< 262	64
2007 Feb 18.16	23.85	VLA	22.50	1168	118
2007 Feb 18.18	23.87	VLA	8.46	303	63
2007 Feb 18.21	23.90	VLA	14.94	798	182
2007 Feb 18.27	23.96	CARMA	95	2400	700
2007 Feb 21.05	26.74	VLA	14.94	1101	148
2007 Feb 22.21	27.90	VLA	4.86	308	78
2007 Feb 23.07	28.76	VLA	1.46	< 984	804
2007 Feb 25.16	30.85	VLA	22.50	839	73
2007 Feb 27.20	32.89	VLA	1.46	< 978	639
2007 Mar 01.22	34.91	VLA	4.86	< 322	95
2007 Mar 01.24	34.93	VLA	14.94	432	149
2007 Mar 01.28	34.97	VLA	8.46	414	66
2007 Mar 01.30	34.99	VLA	22.50	788	74
2007 Mar 13.18	46.87	VLA	1.46	< 1078	739
2007 Mar 15.20	48.89	VLA	4.86	229	49
2007 Mar 15.22	48.91	VLA	8.46	443	59
2007 Mar 21.22	54.91	VLA	4.86	262	52
2007 Mar 21.26	54.95	VLA	8.46	473	44
2007 Mar 23.08	56.77	VLA	22.50	559	161
2007 Mar 25.15	58.84	VLA	1.46	< 580	280
2007 Apr 02.08	66.77	VLA	4.86	226	57
2007 Apr 02.12	66.81	VLA	8.46	345	48
2007 Apr 02.16	66.85	VLA	1.46	< 680	480
2007 Apr 02.20	66.89	VLA	14.94	530	137
2007 Apr 02.24	66.93	VLA	22.50	568	137
2007 Apr 21.13	85.82	VLA	1.46	< 1200	570
2007 Apr 21.18	85.87	VLA	4.86	302	55
2007 Apr 22.18	86.87	VLA	8.46	403	56
2007 Apr 22.99	87.68	VLA	22.50	615	167
2007 Apr 23.02	87.71	VLA	14.94	< 450	226
2007 May 15.03	109.72	VLA	8.46	267	42
2007 May 17.00	111.69	VLA	1.46	< 556	278
2007 May 18.81	113.50	VLA	4.86	< 290	145
2007 May 19.91	114.60	VLA	14.94	< 1440	720
2007 May 20.04	114.73	VLA	22.50	< 176	88
2007 Jul 04.76	160.45	VLA	8.46	145	33
2007 Jul 04.80	160.49	VLA	4.86	174	45
2007 Jul 04.85	160.54	VLA	1.46	< 162	160
2007 Aug 03.87	190.56	VLA	22.50	< 446	223
2007 Aug 11.68	198.37	VLA	4.86	< 100	42

Table 3—Continued

Date of observation	Days since explosion	Telescope	Frequency in GHz	Flux density μJy	Error μJy
2007 Aug 11.72	198.41	VLA	8.46	166	46
2007 Aug 13.71	200.40	VLA	14.94	< 350	169
2007 Sep 08.64	226.33	VLA	4.86	< 141	57
2007 Oct 04.52	252.21	VLA	8.46	148	60
2007 Oct 04.60	252.29	VLA	4.86	203	34
2007 Nov 18.39	297.08	VLA	8.46	111	19
2007 Nov 18.48	297.17	VLA	4.86	161	23
2008 Jan 02.27	341.96	VLA	8.46	64	18
2008 Jan 02.35	342.04	VLA	4.86	133	21

Table 4. Optical/X-ray Afterglow Model Fits

Parameters	Models			
	Single powerlaw		Broken powerlaw	
	same slope	independent slope	same slope	independent slope
α_1	1.80 ^a	$\alpha_1^X(1.85)$, $\alpha_1^O(1.80)$	1.73 ± 0.02	$\alpha_1^X(1.76 \pm 0.30)$, $\alpha_1^O(1.73 \pm 0.02)$
α_2	$2.49^{+0.85}_{-0.18}$	$2.49^{+0.86}_{-0.18}$
t_b (days)	$3.8^{+2.6}_{-0.4}$	$3.8^{+2.6}_{-0.4}$
$\chi^2_{\text{r}}(\text{Total})$	2.23 (99 d.o.f.)	2.25 (98 d.o.f.)	1.30 (97 d.o.f.)	1.31 (96 d.o.f.)
$\chi^2_{\text{r}}(\text{X-ray})$	0.88 (22 d.o.f.)	0.87 (22 d.o.f.)	1.32 (20 d.o.f.)	1.31 (20 d.o.f.)
$\chi^2_{\text{r}}(R\text{-band})$	2.22 (52 d.o.f.)	2.21 (52 d.o.f.)	1.54 (52 d.o.f.)	1.54 (52 d.o.f.)
$\chi^2_{\text{r}}(i'\text{-band})$	3.43 (25 d.o.f.)	3.59 (24 d.o.f.)	0.77 (25 d.o.f.)	0.81 (24 d.o.f.)

Note. — All fits were performed jointly to constrain the relevant decay indices and break time to be the same in all bandpasses. All errors quoted are 90% confidence intervals.

^aThe poor quality of the overall fit precludes meaningful estimates of the 90% confidence intervals.

Table 5. Comparison between Wind and ISM model

parameters	ISM		Wind		Wind-fixed ϵ_e	
	with IC	no IC	with IC	no IC	with IC	no IC
$E_{K,\text{iso}}(10^{52}\text{erg})^a$	$6.45^{+1.03}_{-0.24}$	$14.57^{+3.20}_{-4.01}$	$0.29^{+0.43}_{-0.07}$	$0.15^{+90.0}_{-0.08}$	$1.25^{+0.02}_{-0.17}$	$0.41^{+0.29}_{-0.01}$
θ_j (rad)	$0.23^{+0.01}_{-0.01}$	$0.12^{+0.02}_{-0.01}$	$0.36^{+0.02}_{-0.02}$	$0.33^{+90.0}_{-0.04}$	$0.24^{+0.01}_{-0.02}$	$0.22^{+0.01}_{-0.01}$
p	$2.45^{+0.01}_{-0.02}$	$2.11^{+0.02}_{-0.01}$	$2.17^{+0.01}_{-0.01}$	$2.14^{+0.84}_{-0.01}$	$2.25^{+0.01}_{-0.01}$	$2.18^{+0.01}_{-0.03}$
ϵ_e	$0.27^{+0.03}_{-0.01}$	$0.13^{+0.03}_{-0.02}$	$0.99^{+0.01}_{-0.13}$	$0.77^{+0.02}_{-0.74}$	0.4	0.4
$\epsilon_B(\%)$	$2.77^{+0.44}_{-0.75}$	$99.99^{+0.1}_{-0.0}$	$6.78^{+4.11}_{-7.28}$	$100^{+0.00}_{-98.0}$	$3.73^{+0.87}_{-0.03}$	$100^{+0.00}_{-9.90}$
n or A_\star ^b	$42.07^{+1.59}_{-3.86}$	$4.43^{+0.62}_{-0.20}$	$2.81^{+0.55}_{-0.15}$	$0.99^{+0.03}_{-0.30}$	$3.52^{+0.02}_{-0.43}$	$1.00^{+0.12}_{-0.02}$
t_{jet} (days)	$3.69^{+0.03}_{-0.07}$	$1.61^{+0.04}_{-0.08}$	$7.29^{+0.07}_{-1.09}$	$6.87^{+1.73}_{-3.12}$	$3.34^{+0.10}_{-0.01}$	$3.47^{+0.03}_{-0.08}$
t_{nonrel} (days)	$53.45^{+0.52}_{-0.88}$	$91.74^{+2.30}_{-4.02}$	$27.45^{+1.40}_{-2.08}$	$30.88^{+7.80}_{-9.20}$	$30.03^{+1.17}_{-0.20}$	$36.68^{+0.02}_{-1.07}$
t_{cool} (days)	$8.49^{+0.62}_{-1.72}$	$4.59^{+0.17}_{-0.11}$	$28.40^{+0.73}_{-3.70}$	$30.89^{+0.20}_{-18.10}$	$18.13^{+2.24}_{-1.13}$	$31.37^{+1.04}_{-1.80}$
A_V	7.4×10^{-8}	0.06	0.08	0.11	4.0×10^{-7}	0.08
Fit statistic	592.018	633.022	556.261	575.359	584.854	588.959
$\chi^2/d.o.f.$	$\frac{326.14}{186}$	$\frac{411.42}{186}$	$\frac{254.71}{186}$	$\frac{298.52}{186}$	$\frac{292.66}{187}$	$\frac{335.44}{186}$

^aIsotropic kinetic energy at the time when $\nu_c = \nu_m$.

^bDensity n for ISM model in cm^{-3} and A_\star for wind model.

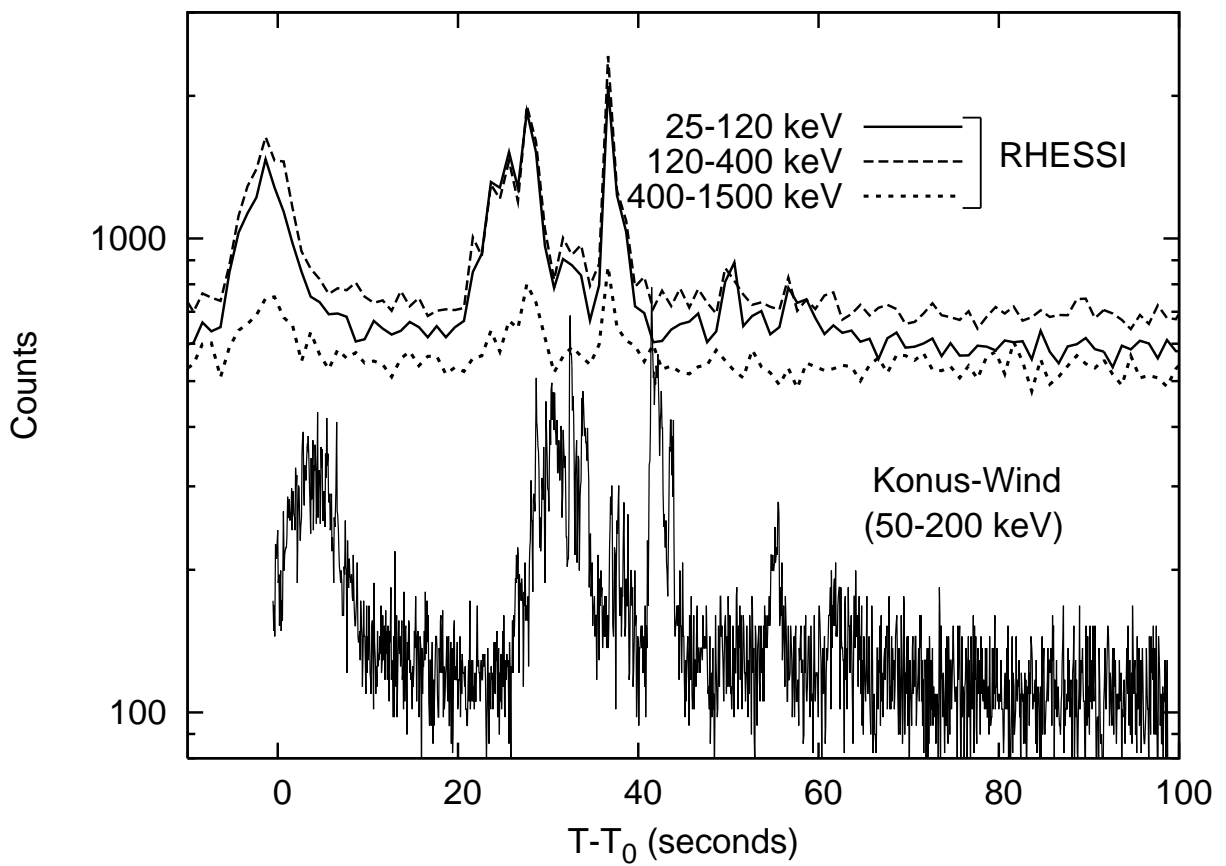


Fig. 1.— Plot of RHESSI data and Konus-Wind data. Their peaks are shifted by 8s because of the difference in light travel time between the two instruments. RHESSI recorded the burst explosion time (T_0) to be 07:20:42 UT and Konus-Wind measured it to be 07:20:50.

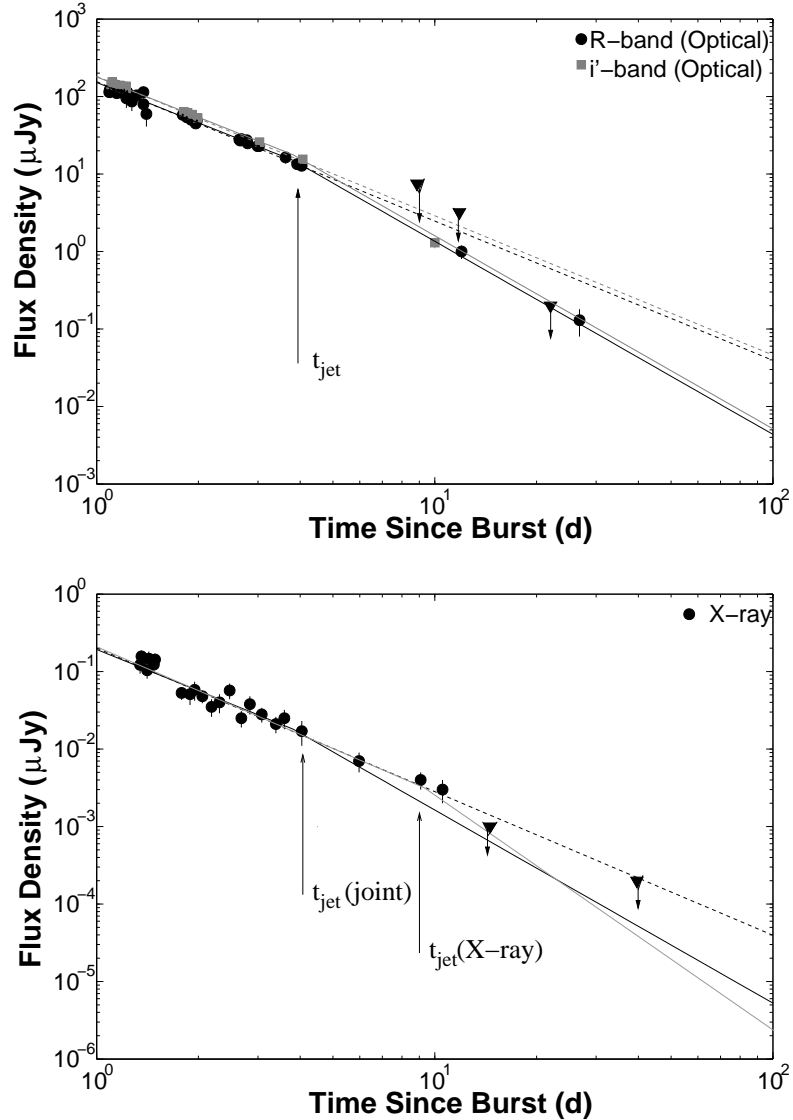


Fig. 2.— *Top*: Optical (R - and i' -band) light curves of GRB 070125 as a result of joint optical and X-ray fits. Best-fit single power-law models are shown with dashed lines, while the broken power-law models are shown in solid lines. It is clear that in the optical bands, a broken power-law (indicating a jet break) is strongly favored. *Bottom*: X-ray light curve of GRB 070125, the the joint fit to optical and X-ray data. Again the single power-law model is shown as a dashed line, while the broken power-law model is shown as a solid line. Grey solid line indicates the independent fit to X-ray data. The independent fit is consistent with the joint fit in the optical bands but shifts the jet break to $\sim 9 - 10$ days. We discuss this in §3.1 and §5.

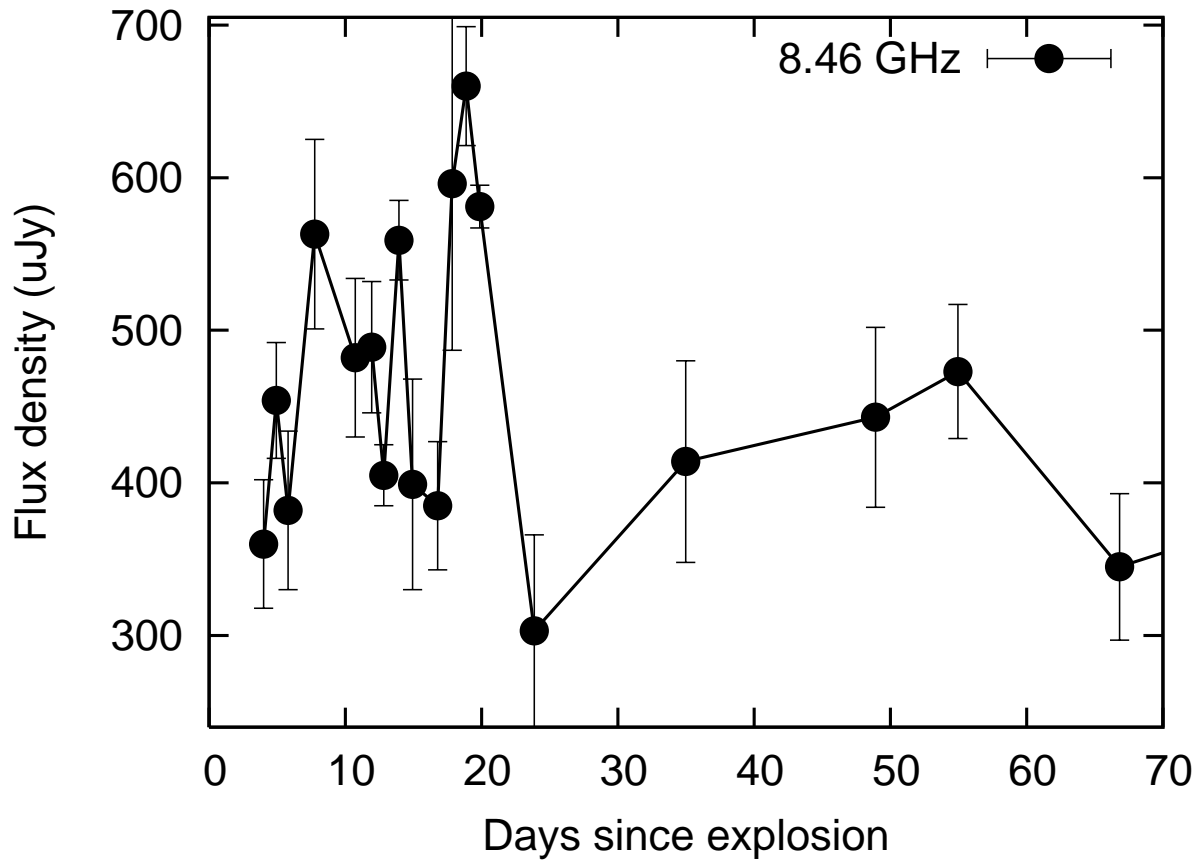


Fig. 3.— Long term light curve at 8.46 GHz showing evidence of interstellar scintillation. This scintillation is refractive in nature and starts dominating once diffractive scintillation quenches (see text for more details).

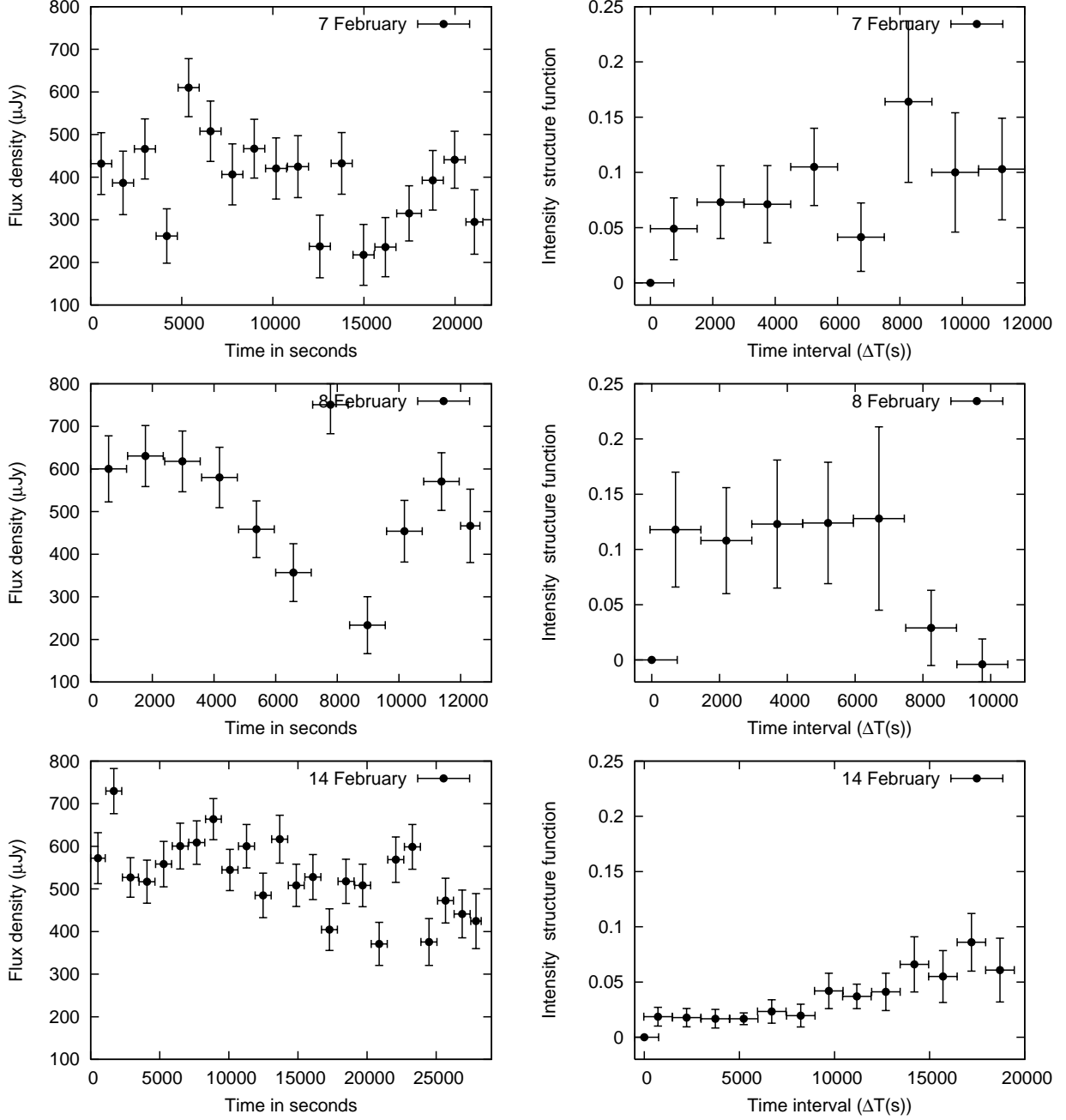


Fig. 4.— Left panel: Lightcurves of the short timescale variations on 7, 8 and 20 February 2007. The data were sampled at intervals of 20 mins. Right panel: Structure functions of the intensity fluctuations on 7, 8 and 14 February 2007. The bias of the thermal noise fluctuations, which adds in quadrature to the source variations in the structure function, has been subtracted.

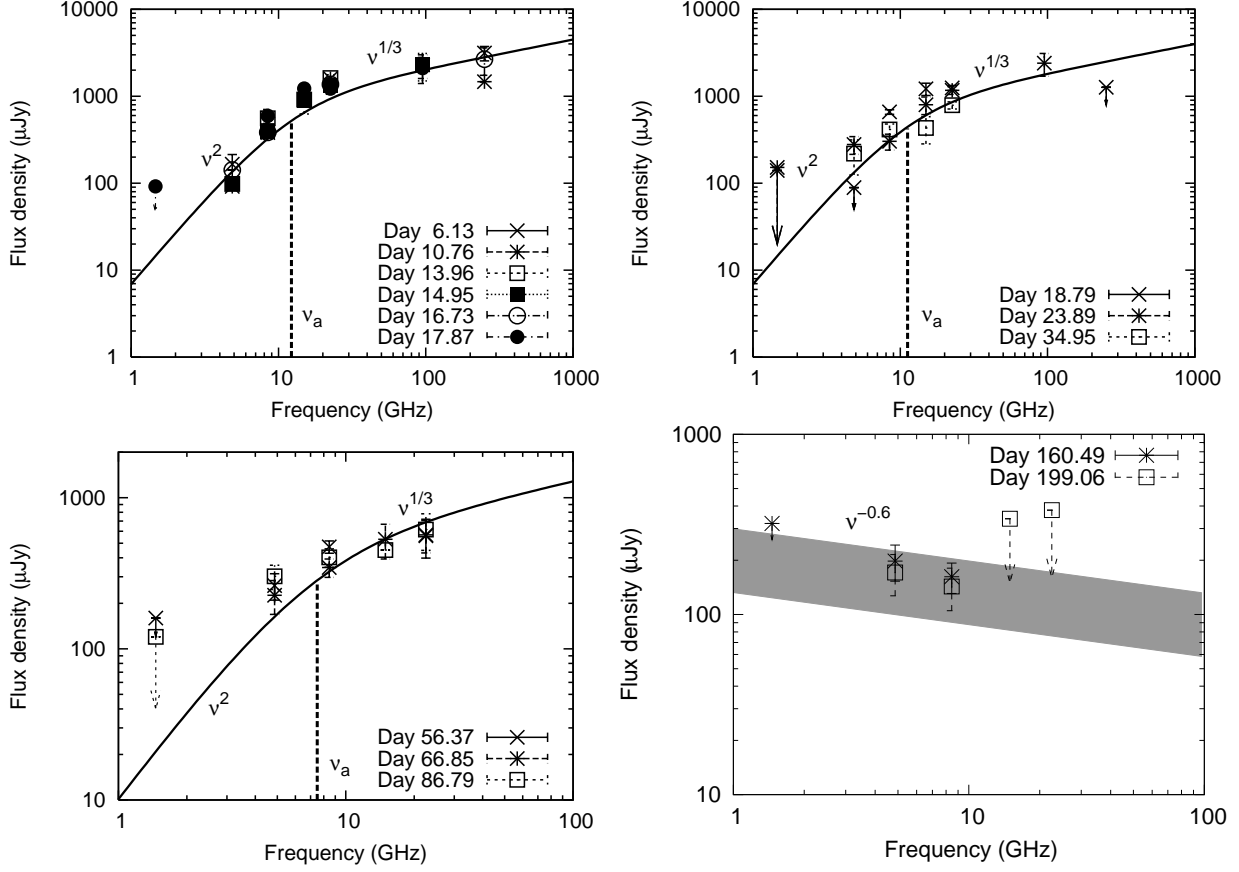


Fig. 5.— Radio spectra of GRB 070125. We combined spectra between days 6–17, 18–34, 56–86 and 160–200 and extracted the best fit ν_a . Between day 160–200 the spectrum is in the optically thin phase, ν_a is below the observed frequencies. The grey area indicates the uncertainty region for the powerlaw index slope.

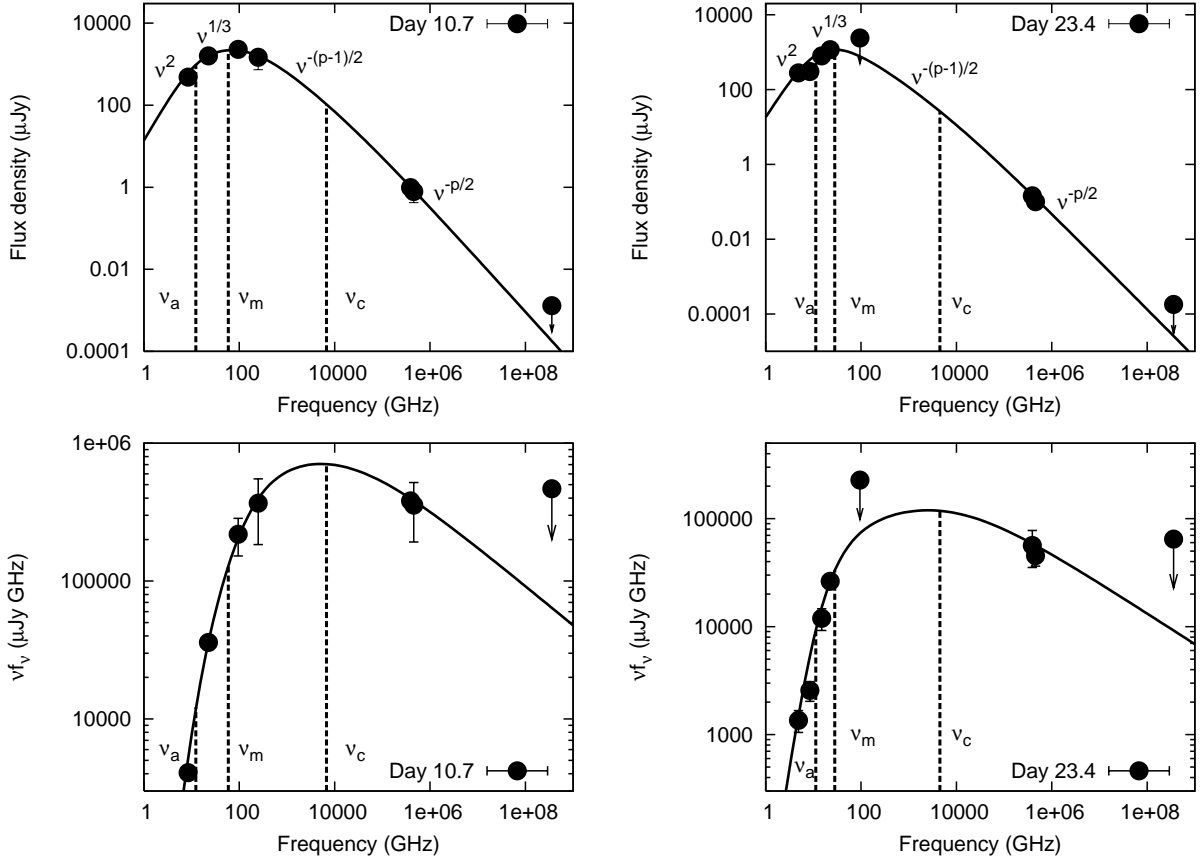


Fig. 6.— Spectra on day 10.7 and day 23.4. We fit a smooth function for the GRB afterglow model and derive the F_{\max} , ν_a , ν_m , and ν_c parameters. The plots at the bottom are νF_ν plots. For slow cooling the flux should peak at ν_m and the total power (νF_ν) should peak at ν_c .

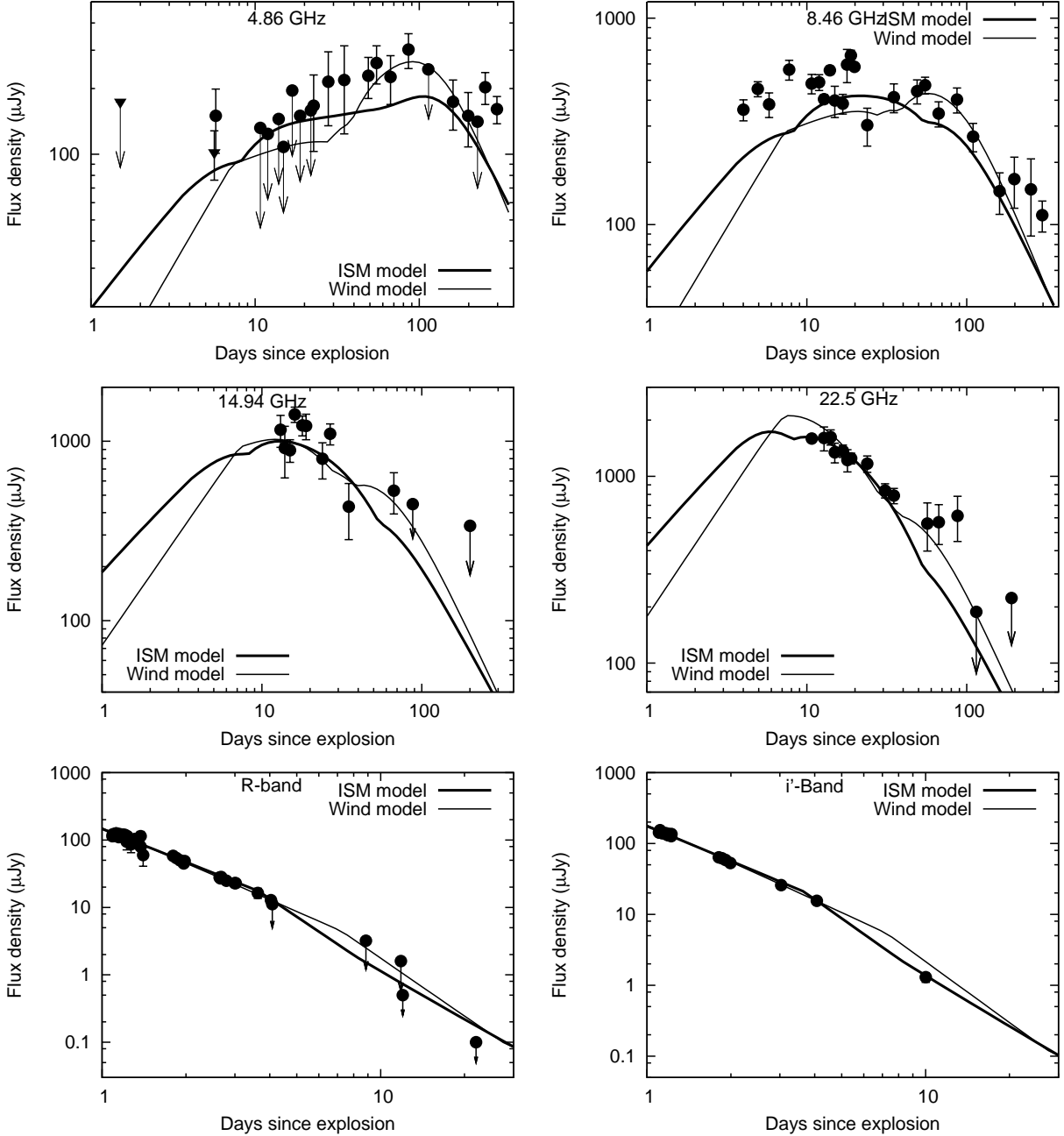


Fig. 7.— Broadband modeling plots for the ISM model as well as the Wind model. We show light curves in 8.46 GHz, 4.86 GHz, R band, and i' band dataset. The darker line is for the ISM model and the Wind model is plotted with a thin line. The fits in the radio bands are good, probably because of scintillation effects.

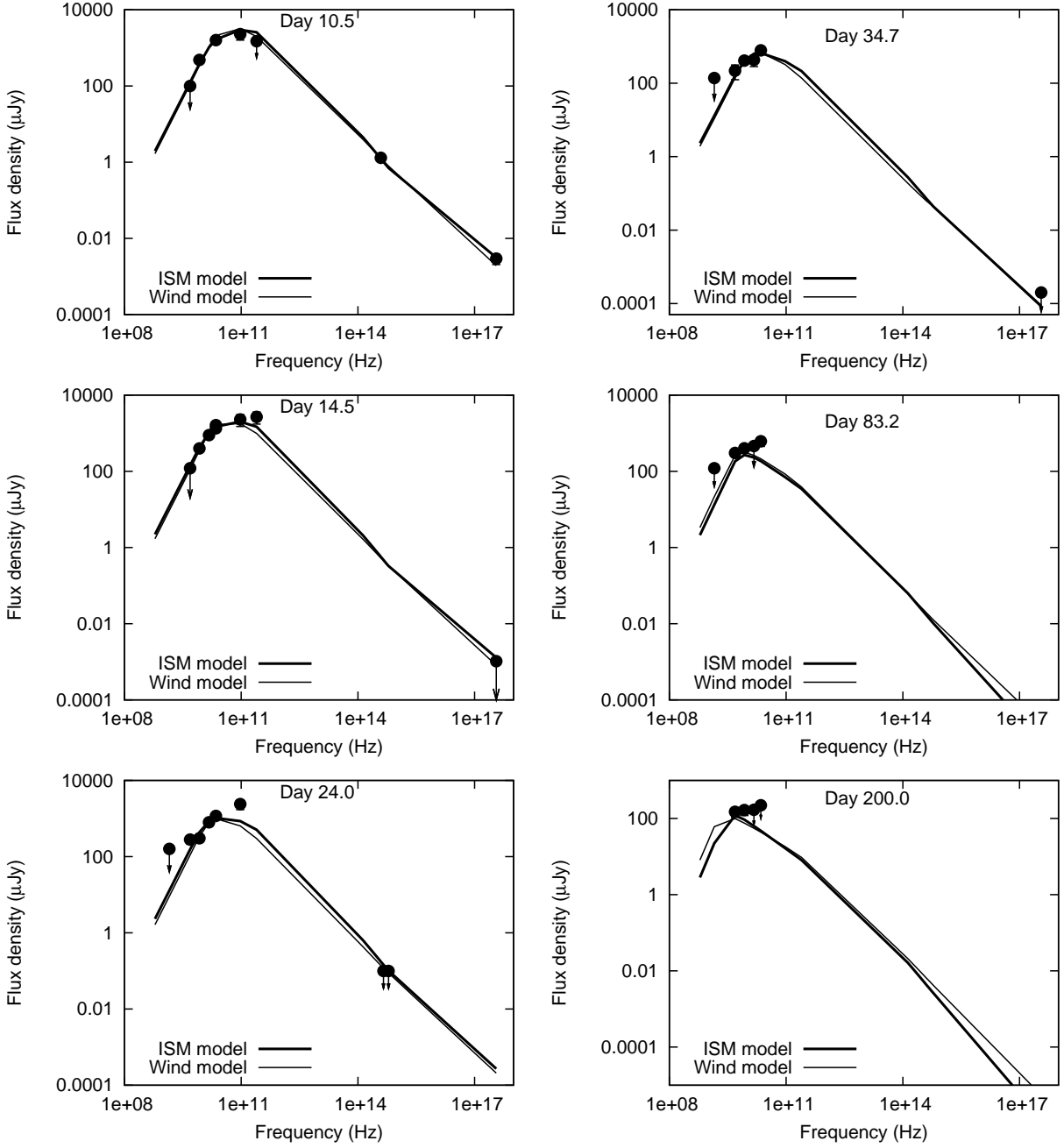


Fig. 8.— Broad band spectra at various days. The thick solid line is the ISM model and the thin solid line represents the Wind model. The peak flux density is well constrained due to submm observations. Both the models give equally good fits.

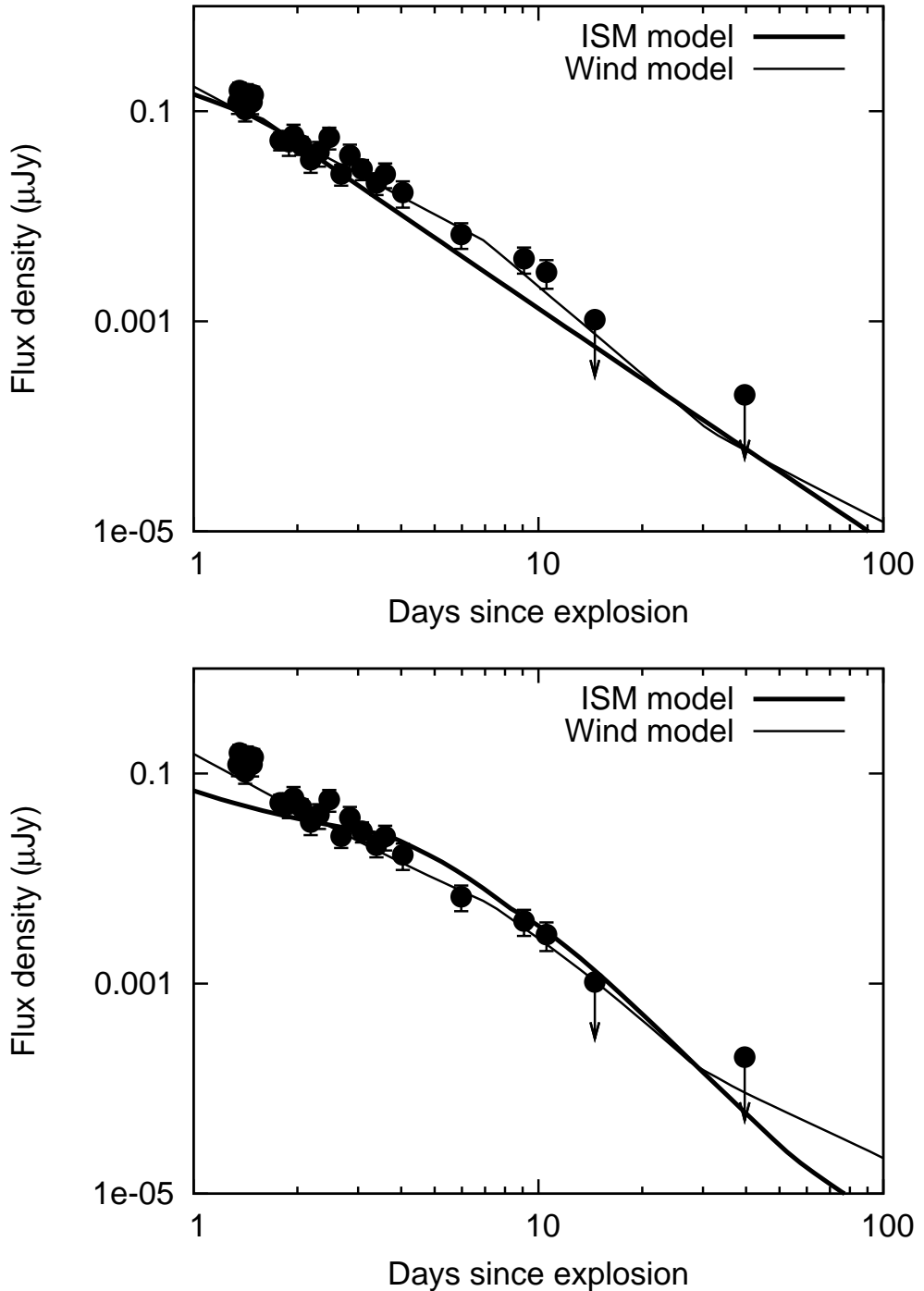


Fig. 9.— X-ray plot only with the pure synchrotron model. The lower figure includes inverse Compton effects. The IC effects start to dominate after 2.5 days.

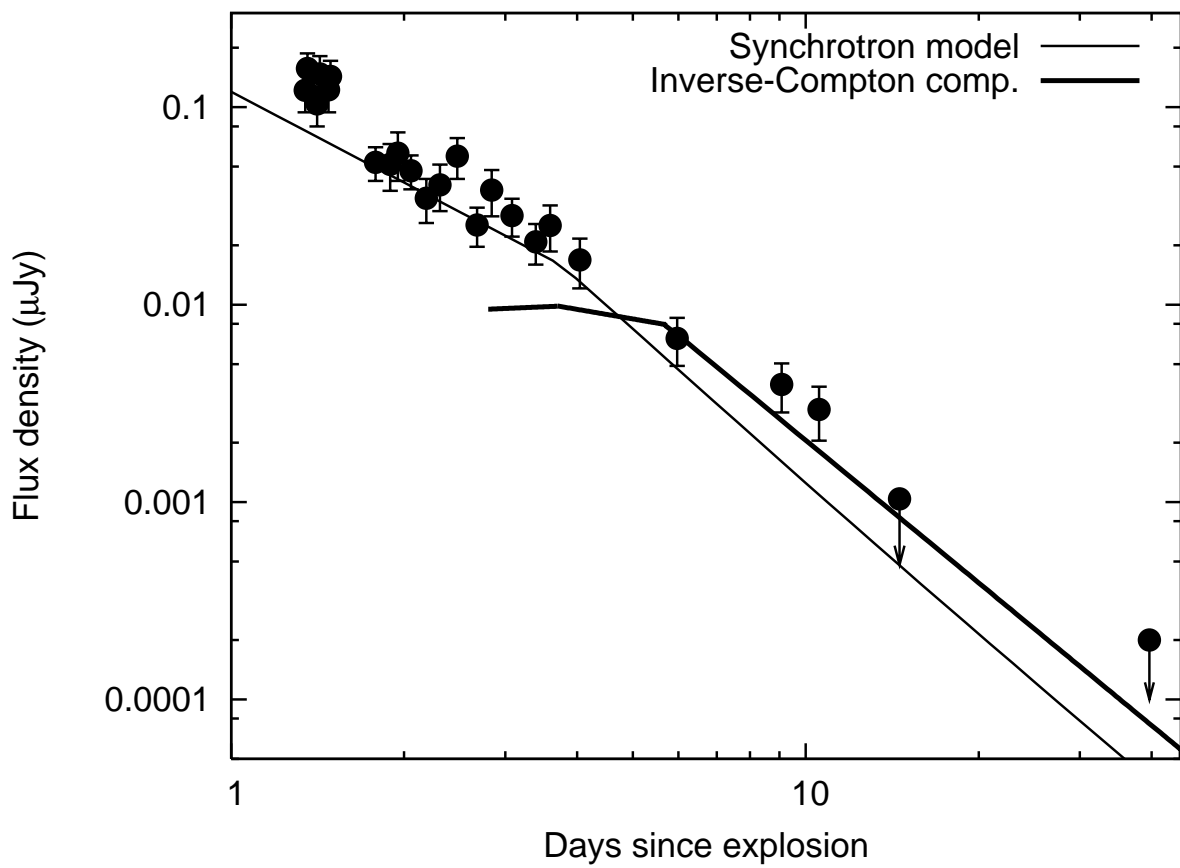


Fig. 10.— Contribution of IC in the synchrotron model. The thin line represents the broadband model with the synchrotron component only. The thick line represents the IC light curve.